CHEMISTRY OF MATERIALS

Article

pubs.acs.org/cm

From 'Green' Aerogels to Porous Graphite by Emulsion Gelation of Acrylonitrile

Anand G. Sadekar,[†] Shruti S. Mahadik,[†] Abhishek N. Bang,[†] Zachary J. Larimore,[‡] Clarissa A. Wisner,[†] Massimo F. Bertino,*[,§] A. Kaan Kalkan,*[,∥] Joseph T. Mang,*[,⊥] Chariklia Sotiriou-Leventis,*[,†] and Nicholas Leventis*[,†]

[†]Department of Chemistry, [‡]Department of Mechanical Engineering, Missouri University of Science and Technology, Rolla, Missouri 65409, United States

[§]Department of Physics, Virginia Commonwealth University, Richmond, Virginia 23284, United States

[∥]Department of Mechanical and Aerospace Engineering, Oklahoma State University, Stillwater, Oklahoma 74078, United States

[⊥]Los Alamos National Laboratory, Los Alamos, New Mexico 87545, United States

Supporting Information

ABSTRACT: Porous carbons, including carbon (C-) aerogels, are technologically important materials, while polyacrylonitrile (PAN) is the main industrial source of graphite fiber. Graphite aerogels are synthesized herewith pyrolytically from PAN aerogels, which in turn are prepared first by solution copolymerization in toluene of acrylonitrile (AN) with ethylene glycol dimethacrylate (EGDMA) or 1,6-hexanediol diacrylate (HDDA). Gelation is induced photochemically and involves phase-separation of "live" nanoparticles that get linked covalently into a robust 3D network. The goal of this work was to transfer that process into aqueous systems and obtain similar nanostructures in terms of particle sizes, porosity, and surface areas. That was accomplished by forcing the monomers into (micro)emulsions, in essence inducing phase-separation of virtual primary particles before polymerization. Small angle neutron scattering (SANS) in combination with location-of-initiator control experiments support that monomer reservoir droplets feed polymerization in ~3 nm radius micelles yielding eventually large (~60 nm) primary particles. The latter form gels that are dried into macro-/mesoporous aerogels under ambient pressure from water. PAN aerogels by either solution or emulsion gelation are aromatized (240 °C, air), carbonized (800 °C, Ar), and graphitized (2300 °C, He) into porous structures (49−64% v/v empty space) with electrical conductivities >5× higher than those reported for other C-aerogels at similar densities. Despite a significant pyrolytic loss of matter (up to 50−70% w/w), samples shrink conformally (31−57%) and remain monolithic. Chemical transformations are followed with CHN analysis, ^{13}C NMR, XRD, Raman, and HRTEM. Materials properties are monitored by SEM and N_2-sorption. The extent and effectiveness of interparticle connectivity is evaluated by quasi-static compression. Overall, irrespective of the gelation method, PAN aerogels and the resulting carbons are identical materials in terms of their chemical composition and microstructure. Although cross-linkers EGDMA and HDDA decompose completely by 800 °C, surprisingly their signature in terms of different surface areas, crystallinity, and electrical conductivities is traced in all the pyrolytic products.

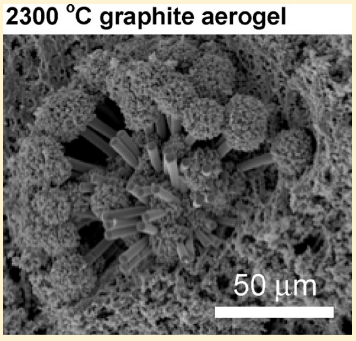

KEYWORDS: *polyacrylonitrile, emulsion polymerization, aerogel, carbon, graphite*

1. INTRODUCTION

Open-pore monolithic carbons are useful as adsorbers,[1] catalyst supports,[2] separation media,[3] electrodes for batteries and fuel cells,[4] and even as materials for hydrogen storage.[5] That class of materials includes carbon (C-) aerogels, which are prepared by pyrolytic carbonization (typically in the 800−1300 °C range) of organic (polymeric) aerogels. Pyrolysis is energy intensive, but the overall cost of C-aerogels is also compounded by typical aerogel-related issues, namely expensive solvent exchanges and also drying using supercritical fluid (SCF) CO_2.[6] Thus, not surprising, of the various carbonizable polymzeric aerogels that include polyurethanes,[7] polyureas,[8] polybenzoxazines,[9] and polyimides,[10] the first-introduced, base-catalyzed aqueous gelation of resorcinol with formaldehyde (RF) still remains the prevalent route to C-aerogels,[11] despite the long (up to a week) process.[12] The resulting C-aerogels preserve the mesoporosity of their RF aerogel precursors, but from an applications perspective macroporosity is also important (e.g., for low flow-through mass transfer resistance). In that regard, a large body of literature is devoted to methods that induce macroporosity in RF aerogels and includes the following: use of low catalyst-to-monomer concentrations;[11] use of acid catalysis (acetic acid in aqueous media);[13] hard templating with polystyrene microspheres;[14] soft templating with surfactants[15]

Received: June 15, 2011
Revised: November 19, 2011
Published: December 14, 2011

ACS Publications © 2011 American Chemical Society

or surfactant-stabilized oil droplets (the latter are referred to as high internal phase emulsions or HIPEs);[16] and conformally coating the entire nanostructure with thermally detachable polyurea that, once free, finds itself above its melting point and causes local structural collapse of the RF network, creating macropores.[17] Moreover, with an eye into extending the possible applications of carbon aerogels into novel applications (e.g., lithium intercalation electrodes[18]), conversion of C- to graphite aerogels has been also considered. For this, it is known that certain transition metals (e.g., Fe, Co, Ni, Mn) catalyze graphitization of carbon.[19] Thus, graphite aerogels have been produced by pyrolysis of RF aerogels doped with the corresponding metal ions,[20] whereas the metal catalyst is formed in situ by carbothermal reduction of the dopant ions.[21] Direct graphitization would prevent contamination with elements that may compromise later use (e.g., because of leakage currents or unwanted catalytic activity).

Based on the above, a desirable route to C-aerogels would entail a high-yield carbonizable and subsequently graphitizable polymer but above all a time-efficient water-based gelation process followed by ambient pressure drying yielding meso/macroporous materials. With regards to the first requirement, polyacrylonitrile (PAN), the primary industrial source of graphite fiber for reinforcing composites in applications from high-end luggage to major automotive and aerospace components,[22] should comprise a suitable C-aerogel precursor. However, the water solubility of the monomer, acrylonitrile (AN), is low (~7 g per 100 mL of water at 20 °C), while the polymer, PAN, is linear and readily soluble in organic media. Therefore, from a bottom-up perspective direct solution gelation of AN in water is not easy, while highly concentrated solutions of PAN in organic media may look like gels, but upon drying, even with SCF CO_2, such gels deswell and collapse in order to maximize the noncovalent interactions (e.g., van der Waals) among the polymeric strands.[23a] Nevertheless, successful top-down pathways to organic aerogels from the preformed linear polymers have been described. Historically, those methods are traced to S. Kistler's preparation of nitrocellulose aerogels by inducing phase separation via slow addition of benzene (a nonsolvent) in ethanolic solutions of the polymer.[24] Similarly, phase separation can be induced by slow cooling of concentrated polymer solutions, and that method has been employed for polystyrene,[25] cellulose,[26] and also polyacrylonitrile aerogels.[27] The nanostructure of those aerogels is mostly fibrous, and since the polymers are linear, covalent linking is low, monoliths are inherently mechanically weak, and we speculate that fiber entanglement plays a significant role in their integrity.[28] Thus, one of the most interesting uses of PAN aerogels is not dealing with monoliths at all but rather with films made by grafting PAN on carbon nanotubes that in turn are deposited on microfibrous carbon paper; the PAN aerogel layer is a few nm thick and consists of entangled fibers.[29] Here, moving along the importance of interparticle covalent bridging in the mechanical properties of aerogels,[30] we have opted for a bottom-up process, whereas PAN aerogels are synthesized from monomers through an aqueous route. For comparison purposes, PAN aerogels have been also synthesized through solution polymerization and serve as reference.

For those objectives, PAN was cross-linked with two variable-length bifunctional acrylates, EGDMA and HDDA, borrowed from the extensive literature on macroporous chromato graphic stationary phases.[31] Although copolymerization of AN with EGDMA or HDDA is straightforward, relevant reports are scarce[32] and not related to aerogels or porous carbons. During

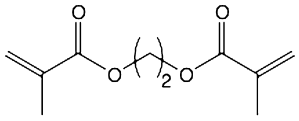

EGDMA

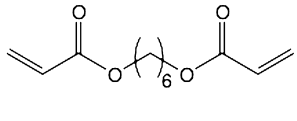

HDDA

solution polymerization in toluene, cross-linking of PAN with EGDMA or HDDA decreases the solubility of the developing polymeric strands and causes phase-separation of presumably radical-terminated colloidal nanoparticles that get linked covalently among themselves into robust porous 3D networks. That process is transferred into emulsions in water,[33] whereas surfactant micelles play the role of reaction nanovessels, hence they can be thought of as virtual primary particles growing into real particles that in turn get cross-linked to a network similar to the one obtained by solution polymerization. In all cases except one, stable, clear (micro)emulsions of AN and each of the cross-linkers were obtained with combinations of cationic surfactant ***surf-1*** and nonionic Triton X-100. A free-radical process was initiated with a water-soluble dicarboxylate derivative of 2,2′-azobisisobutyrolitrile (AIBN) introduced as a surfactant itself (***surf-AIBN***).

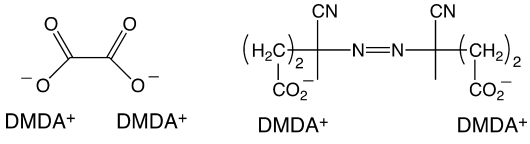

DMDA⁺ DMDA⁺ DMDA⁺ DMDA⁺

surf-1 ***surf-AIBN***

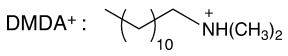

Surfactants have been employed numerous times in aerogel synthesis, mainly in order to reduce surface tension for efficient drying,[34] but also in reverse emulsions for the synthesis of carbon aerogel spheres from RF aerogels,[35] and as templating agents for ordered mesoporous silicas,[36] as well as macroporous carbons.[15,16] Particularly relevant to this work is the recent use of HIPEs by Silverstein for the synthesis of porous PAN and its pyrolytic conversion to porous monolithic carbons.[37] Recognizing the finite solubility of AN in water, as well as the need for molecular cross-linking in terms of imparting strength in PAN, those authors used two initiators, one water-soluble and one lipophilic, along with a nonionic surfactant stabilized suspension of the monomers (AN and divinylbenzene) in water. The resulting materials are cellular (pore sizes in the order of 10 μm), and they resemble certain porous structures reported by Antonietti in similar emulsions using water-soluble monomers[38] and are distinctly different from the ones reported herewith.

Wet-gels described herewith from either the solution (toluene) or the emulsion (water) route include macropores (~100−300 nm in diameter) that withstand the surface tension forces of evaporating solvents and thereby are dried into aerogels under ambient pressure. The latter are indistinguishable from samples obtained via the conventional SCF CO_2 route. After carbonization at 800 °C, C-aerogels from either solution or emulsion polymerization are again strictly identical. Differences among samples are traced only to the cross-linkers (EGDMA versus HDDA). Upon further pyrolysis in the 2200−2300 °C range, samples remain monolithic, consist of graphite, and exhibit electrical conductivities significantly higher (>5×) than those reported previously for carbon aerogels at the same

dx.doi.org/10.1021/cm202975p | *Chem. Mater.* 2012, 24, 26−47

Table 1. Formulations of Emulsion- (W-) Based PAN Aerogels

sample	AN (mL) [mol]	X-linker[d] (mL) [mol]	total AN+X-linker (mL)	surfactants: *surf-AIBN* (mL)	*surf-1* (mL)	Triton X-100 (g)	SDS (g)	water from surfactant stock solution (mL)	additional water (mL)	total water (mL)	total volume (mL)
W-E-50-40[a]	20.0 [0.305]	20.0 [0.106]	40.0	10	0	10	15	9	51	60	126.0
W-E-50-50[b]	25.0 [0.382]	25.0 [0.133]	50.0	10	0	25	0	9	41	50	126.0
W-E-75-40[b]	30.0 [0.458]	10.0 [0.053]	40.0	10	45	10	0	39	21	60	126.0
W-E-75-50[b]	37.5 [0.572]	12.5 [0.066]	50.0	10	45	10	0	39	11	50	126.0
W-H-50-40[b]	20.0 [0.305]	20.0 [0.088]	40.0	10	45	10	0	39	21	60	126.0
W-H-50-50[b]	25.0 [0.382]	25.0 [0.110]	50.0	10	45	10	0	39	11	50	126.0
W-H-75-40[b]	30.0 [0.458]	10.0 [0.044]	40.0	10	45	10	0	39	21	60	126.0
W-H-75-50[b]	37.5 [0.572]	12.5 [0.055]	50.0	10	45	10	0	39	11	50	126.0
W-H-75-50*[a,c]	37.5 [0.572]	12.5 [0.055]	50.0	10	0	10	15	9	41	50	105.0

[a]Quasi-stable (for a few hours) opaque-white (milky) emulsion. [b]Clear emulsion, stable indefinitely. [c]Sample noted with asterisk was prepared using SDS as surfactant for direct comparison of the micelle size of a clear emulsion, **W-H-75-50**, with SANS. [d]X-Linker: **E-**, EGDMA; **H-**, HDDA.

bulk densities. Materials are characterized with emphasis on the following: (a) the gelation mechanism; (b) ambient pressure drying; and (c) the effect of the two cross-linkers on the materials properties. The emulsion process is referred to as "green", because it includes directly three of the twelve criteria for green chemistry (the rest being implicit or irrelevant):[39] (a) it is water-based; (b) all monomers are incorporated into the final product; and (c) it is less energy intensive than alternatives.

2. EXPERIMENTAL SECTION

Materials. All reagents and solvents were used as received unless noted otherwise. Acrylonitrile (AN), ethylene glycol dimethacrylate (EGDMA), 1,6-hexanediol diacrylate (HDDA), oxalic acid, *N,N*-dimethyldodecylamine, 4,4′-azobis-(4-cyanovaleric acid), Triton X-100, sodium lauryl sulfate (SDS), and 2,2′-azobisisobutyronitrile (AIBN) were purchased from Sigma-Aldrich. AIBN was further purified by recrystallization from methanol. HPLC grade toluene and acetone were purchased from Fisher. Pure USP 200 grain grade ethanol was purchased from Aaper Alcohol and Chemical Co. Siphon grade CO_2 was purchased from Ozarc Gas Co.

*Synthesis of **surf-1**.* Oxalic acid (7.00 g, 0.056 mol) was dissolved in HPLC grade acetone and neutralized with *N,N*-dimethyldodecyl amine (DMDA, 23.71 g, 0.12 mol). Acetone was removed under reduced pressure leaving behind ***surf-1*** as a viscous liquid. ^{13}C NMR ($CDCl_3$) δ (ppm): 169.5, 58.8, 43.9, 32.1, 29.8, 29.8, 29.7, 29.6, 29.5, 27.3, 25.48, 14.3. ***Surf-1*** is water-soluble and was stored as a 33% w/w solution in water (solution density: 0.948 g cm^{-3}).

*Synthesis of **surf-AIBN**.* 4,4′-Azobis-4-cyanovaleric acid (1 g, 3.57 mmol) was dissolved in HPLC grade acetone and neutralized with *N,N*-dimethyldodecyl amine (1.52 g, 7.12 mmol). Acetone was removed under reduced pressure leaving behind a viscous liquid. ^{13}C NMR ($CDCl_3$) δ (ppm): 177.4, 118.5, 72.52, 59.22, 58.10, 43.64, 42.52, 32.10, 29.81, 29.73, 29.53, 27.24, 25.15, 24.35, 23.98, 22.88, 14.41. ***Surf-AIBN*** is water-soluble and was stored as a 10% w/w solution in water (solution density: 0.990 g cm^{-3}).

Synthesis of PAN Aerogels via Emulsion Polymerization. All formulations are summarized in Table 1. Emulsion (i.e., water- (**W-**) based) aerogels are referred to by the AN:(AN+cross-linker) and the monomers:(monomers+solvent) volume ratios (v/v), and are abbreviated as **W-E-xx-yy** or **W-H-xx-yy**, whereas **E-** denotes samples made with EGDMA and **H-** with HDDA as cross-linkers; **xx** stands for the volume percent (% v/v) of AN over total monomers (i.e., AN plus cross-linker); and **yy** stands for the volume percent of total monomers over total monomers plus water. In a typical process, Triton X-100 was dissolved in a predetermined amount of water (Table 1) by vigorous magnetic stirring and heating at about 50 °C. The solution was allowed to cool to room temperature and ***surf-1*** (or in some instances SDS) and ***surf-AIBN*** were added (as solutions according to Table 1). Stirring was continued for another 30 min. All emulsions up to that point were clear colorless and stable indefinitely. Subsequently, the appropriate mixture of acrylonitrile (AN) and cross-linker (EGDMA or HDDA) was added dropwise under vigorous magnetic stirring over a period of 45−60 min. The new emulsions were either transparent or milky-white (see Table 1). Emulsions were transferred into polypropylene molds (Wheaton polypropylene Omni-Vials, 1.0 cm in diameter) and were exposed to UV light using a Dymax Light Curing Systems unit, Model 38100-5000-EC, 400 W (365 nm), changing the angle of exposure frequently until gelation (~300 s). All resulting wet-gels were opaque-white, and they were aged in their molds for 12 h at 55 °C followed by 12 h at 75 °C. As it turns out though, that aging step is not necessary (see Section 3a in Results and Discussion). Subsequently, wet-gels were removed from the molds, washed with water (4 times, allowing 8 h for each cycle), and dried into aerogels at 60 °C for 2 days under ambient pressure. The washing and drying steps have not been optimized time-wise. For control purposes, after washing with water, a series of wet-gels were solvent-exchanged with ethanol (4 times, 8 h per wash cycle) and dried in an autoclave with liquid CO_2 taken out at the end as a SCF.

Synthesis of PAN Aerogels via Solution Polymerization. All formulations are summarized in Table 2. Those aerogels are abbreviated as **S-E-xx-yy** or **S-H-xx-yy**, where **S** denotes solution polymerization, and **E, H, xx**, and **yy** have the same meaning as above. Sols were prepared by dissolving AN, cross-linker (EGDMA or HDDA), and AIBN in toluene at room temperature. Sols were poured into polypropylene molds (Wheaton polypropylene Omni-Vials, Part No. 225402, 1 cm in diameter) and were exposed to UV light using a Dymax Light Curing Systems unit, Model 38100-5000-EC, 400 W (365 nm), changing the angle of exposure frequently until gelation (~300 s). At that point, wet-gels were opaque-white, they were aged in their molds at 55 °C for 12 h, solvent-exchanged with toluene (4 times, 8 h per wash cycle) and ethanol (again 4 times, 8 h per wash cycle), and dried into white PAN aerogels under ambient pressure for 3 days at room temperature.

Conversion of PAN Aerogels to C-Aerogels. PAN aerogel monoliths were initially aromatized at 240 °C for 36 h in air, turning from white to brown. Samples were cooled to room temperature, transferred to an MTI GSL1600X-80 tube furnace, and were heated again under flowing Ar (70 mL min^{-1}) as follows: The temperature was raised to 300 °C (2 h) and maintained there for 1 h, and subsequently it was raised to 800 °C (2 h), and it was maintained at that level for 3 h. At that point, the power to the furnace was disconnected allowing slow cooling back to room temperature (12 h).

Conversion of Carbon Aerogels to Graphite Aerogels. C-aerogel monoliths produced at 800 °C as above were placed in a hot-zone graphite furnace (Thermal Technologies Inc., Model:1000-3060-FP20) under a helium atmosphere. The temperature was raised from room temperature to 400 °C at the rate of 40 °C min^{-1} and then to 2200 or 2300 at 10 °C min^{-1}. Samples were kept at that temperature for a period of 24 h. At the end, the power to the furnace

dx.doi.org/10.1021/cm202975p | *Chem. Mater.* 2012, 24, 26−47

Table 2. Formulations of Solvent- (S-) Based PAN Aerogels

sample	AN (mL) [mol]	X-linker (mL) [mol]	total AN + X-linker (mL)	volume of toluene (mL)	total solution volume (mL)	AIBN (g)
S-E-25-30	1.5 [0.023]	4.5 [0.024]	6	14	20	0.075
S-E-25-40	2.0 [0.031]	6.0 [0.032]	8	12	20	0.100
S-E-25-50	2.5 [0.038]	7.5 [0.040]	10	10	20	0.125
S-E-50−30	3.0 [0.046]	3.0 [0.016]	6	14	20	0.075
S-E-50-40	4.0 [0.061]	4.0 [0.021]	8	12	20	0.100
S-E-50-50	5.0 [0.076]	5.0 [0.027]	10	10	20	0.125
S-E-75-30	4.5 [0.068]	1.5 [0.008]	6	14	20	0.075
S-E-75-40	6.0 [0.092]	2.0 [0.011]	8	12	20	0.100
S-E-75-50	7.5 [0.114]	2.5 [0.013]	10	10	20	0.125
S-H-25-30	1.5 [0.023]	4.5 [0.020]	6	14	20	0.075
S-H-25-40	2.0 [0.031]	6.0 [0.026]	8	12	20	0.100
S-H-25-50	2.5 [0.038]	7.5 [0.033]	10	10	20	0.125
S-H-50−30	3.0 [0.046]	3.0 [0.013]	6	14	20	0.075
S-H-50-40	4.0 [0.061]	4.0 [0.018]	8	12	20	0.100
S-H-50-50	5.0 [0.076]	5.0 [0.022]	10	10	20	0.125
S-H-75-30	4.5 [0.068]	1.5 [0.007]	6	14	20	0.075
S-H-75-40	6.0 [0.092]	2.0 [0.009]	8	12	20	0.100

switched off, and it was allowed to cool to room temperature at its normal rate (overnight).

Methods. Bulk densities (ρ_b) were calculated from the weight and the physical dimensions of the samples. Skeletal densities (ρ_s) were determined with helium pycnometry using a Micromeritics AccuPyc II 1340 instrument. Porosities, Π, as percent empty space, were determined from the ρ_b and ρ_s values via $\Pi = 100 \times [(1/\rho_b)-(1/\rho_s)]/(1/\rho_b)$. Surface areas ($\sigma$) were measured by N_2-sorption porosimetry using a Micromeritics ASAP 2020 Surface Area and Pore Distribution Analyzer. Samples for surface area and skeletal density determinations were outgassed for 24 h at 80 °C under vacuum before analysis. Liquid ^{13}C NMR of monomers were obtained with a 400 MHz Varian Unity Inova NMR instrument (100 MHz carbon frequency). Solid samples after aromatization (heated at 240 °C in air) were characterized by ^{13}C CPMAS solid NMR spectroscopy using the TOSS pulse sequence with broadband proton decoupling and magic angle spinning (at 5 kHz). Samples after carbonization (800 °C) contained no hydrogen and were characterized by one-pulse sequence and magic angle spinning (at 7 kHz). All samples for solids NMR were ground to fine powders and packed into 7 mm rotors. All solids ^{13}C NMR spectroscopy was conducted with a Bruker Avance 300 wide bore NMR spectrometer equipped with a 7 mm CPMAS probe. The operating frequency for ^{13}C was 75.483 MHz. ^{13}C NMR spectra were referenced externally to glycine (carbonyl carbon at 176.03 ppm). The structure of emulsions as well as of the fundamental building blocks of the resulting aerogel microstructures were probed with small-angle neutron scattering (SANS) at the Manuel Lujan Jr. Scattering Center of the Los Alamos National Laboratory, using the time-of-flight, Low-Q Diffractometer (LQD).[40] The scattering data are reported in the absolute units of differential cross section per unit volume (cm^{-1}) as a function of Q, the momentum transferred during a scattering event. In all cases, data were reduced by conventional methods (see Results and Discussion) and corrected for empty cell and background scattering. Scanning Electron Microscopy (SEM) was conducted with samples coated with Au−Pd using a Hitachi S-4700 field emission microscope. Transmission Electron Microscopy (TEM) was conducted with a FEI Tecnai F20 instrument employing a Schottky field emission filament operating at a 200 kV accelerating voltage. C-aerogel samples were finely ground by hand in a mortar with a pestle and placed in 5 mL glass vials, isopropanol (3 mL) was added, and the vials were ultrasonicated for 20 min to disperse the small particles in the solvent. After removing from the ultrasonic bath and just before particle settling was complete, a single drop was taken and placed on a 200 mesh copper grid bearing a lacey Formvar/carbon film. Each grid was allowed to air-dry before been used for microscopy. At least different 6 areas/particles were examined on each sample to ensure that the results were uniform over the whole sample. Images were processed with Image J, a freely available software that allows measuring the distance between the lattice fringes. Four-point-probe conductivity measurements were carried out with an instrument consisting of an Alessi CPS-06 Contact Probe Station with four point probe head, a Keithley Model 220 programmable current source, and a Model 181 nanovoltmeter. The reliability of the measurements was confirmed with commercially available silicon wafers, indium−tin-oxide films of known sheet resistance, and RF-derived carbon aerogels prepared for this purpose as controls. The conductivity was calculated via Conductivity = 1/Resistivity, where Resistivity = $2\pi \times s \times T_1(t/s) \times C_o(d/s) \times (V/I)$, where s is the distance between electrodes in the probe (0.1588 cm), and $T_1(t/s)$ and $C_o(d/s)$ are geometric correction factors due to the finite thickness (t) and diameter (d) of the samples. For t = 0.703 cm and d = 1.253 cm, (t/s) = 4.42 and (d/s) = 7.88 cm, and $T_1(t/s) = 0.9908$, and $C_o(d/s) = 0.8785$.[41] Discs for electrical conductivity measurements were cut dry with a diamond saw from PAN aerogels cylinders and were processed through pyrolysis as described above. X-ray diffraction (XRD) was performed with powders of the corresponding materials using a PANalytical X'Pert Pro diffractometer with Cu Kα radiation and a proportional counter detector equipped with a flat graphite monochromator. Raman spectroscopy of carbon was conducted with a Jobin-Yvon micro-Raman spectrometer with a 632.8 nm He−Ne laser as the excitation source. Reference graphite and amorphous carbon (carbon black) samples were purchased from Sigma-Aldrich (CAS Nos. 7782-42-5 and 7440-44-0, respectively). The concentration of acrylonitrile in the aqueous phase in water-acrylonitrile-cross-linker mixtures (the cross-linkers are not miscible with water at all) was determined by measuring the refractive index (RI) of the aqueous phase, using a Reichert AR200 Digital Refractometer and a calibration curve that gave the following: $RI@25°C = 9.3075 \times 10^{-4} \times$ (% w/w of AN in water) + 1.3326. All RIs were measured at room temperature and were reduced to 25 °C using a quadratic formula.[42] For the determination of Critical Micelle Concentrations (CMC) we used a Goniometer/Tensiometer from Ramé-Hart Instrument Co., Model-250, F-1 series that employs the hanging pendant drop method, and data were analyzed using the Young−Laplace equation through the instrument software. Elemental analysis (CHN) was conducted with a Perkin-Elmer Model 2400 CHN Elemental Analyzer, calibrated with acetanilide purchased from the National Bureau of Standards. Modulated Differential Scanning Calorimetry (MDSC) was conducted under N_2 and in air from −30 to 300 °C, with a TA Instrument Model 2920 apparatus at a heating rate of 10 °C min^{-1}. For measuring heat capacities, MDSC was run from −30 to 40 °C in the modulated T4P mode at 0.5 °C min^{-1} using 60 s as the modulation period and 1 °C as the modulation amplitude.

dx.doi.org/10.1021/cm202975p | Chem. Mater. 2012, 24, 26−47

Scheme 1. Bottom-up Synthesis of Polymeric Aerogel Monoliths

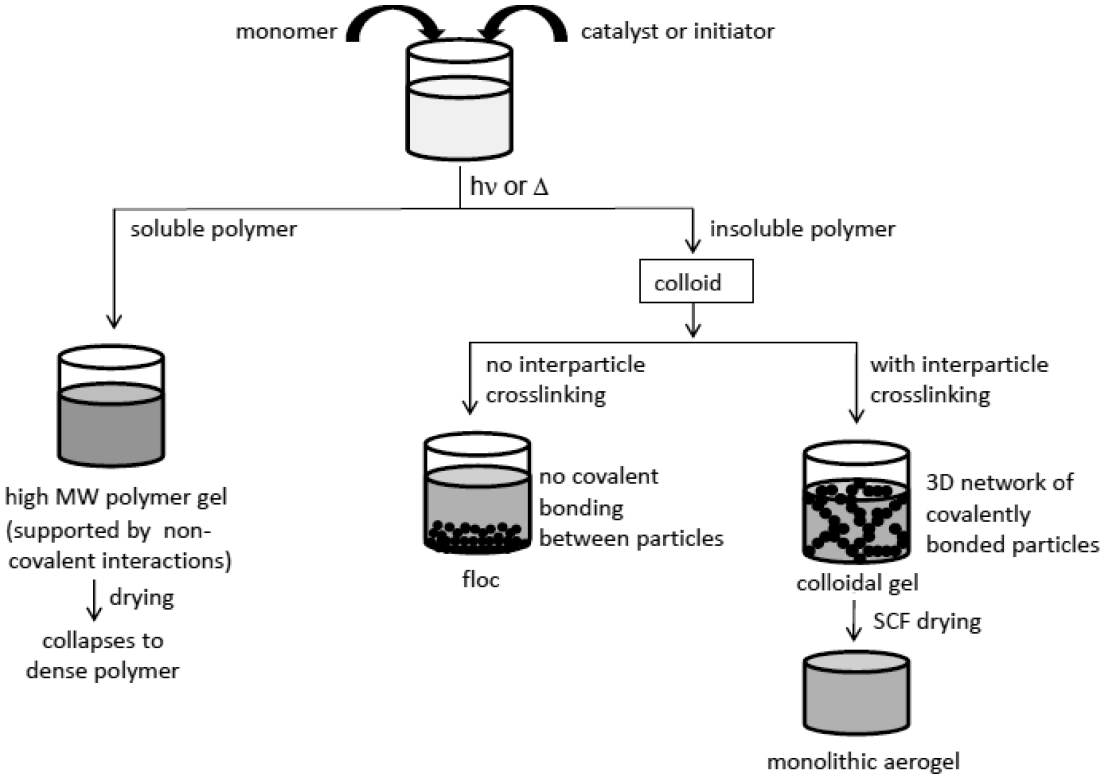

Mechanical characterization (compression testing) was conducted according to the ASTM D695-02a standard on cylindrical specimens (height:diameter = 2:1), using an Instron 3380 machine equipped with either a 100 kN (for **S**-based PAN aerogels) or a 10 kN load cell (for **W**-based PAN aerogels). Typical samples were ~1.0 cm diameter, ~2.0 cm long.

3. RESULTS AND DISCUSSION

3.a. Bottom-up Synthesis of PAN Aerogels. As summarized by Scheme 1, concentrated, highly viscous polymer solutions may be gel-like; however, upon drying there is nothing to prevent collapse driven by noncovalent interactions. On the other hand, if the polymer is insoluble in the polymerization medium, and if the conditions are favorable (solvent, temperature, polymerization kinetics), it may phase-separate into a colloidal solution, which, in the absence of interparticle cross-linking, will eventually form a loose aggregate (like a floc). Such aggregates may occupy the entire volume of the parent colloidal solution but cannot be dried into solid objects. With interparticle cross-linking though, the 3D covalent network will resist collapse upon drying and may yield an aerogel. Typically, phase-separation and interparticle cross-linking are introduced during solution polymerization by enforcing cross-linking at the molecular level with multifunctional monomers. A wide variety of aerogels has been synthesized implicitly or explicitly by that method.[7−12,14,15,17,30]

Alternatively, phase-separation can be introduced *prior to* polymerization with surfactant micelles in water. By analogy to gelation via solution polymerization, it was reasoned that addition of cross-linkers (EGDMA or HDDA) could assist "latex" particles develop interparticle covalent bonds, and the structure would resist collapse upon drying.

Gelation of AN with EGDMA or HDDA is based on eq 1. Solution gelation in toluene proceeds according to Scheme 1, as

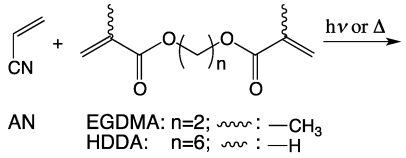

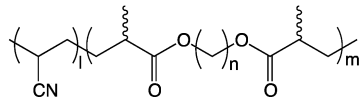

(1)

W- or **S-**, **E-** or **H-xx-yy**

planned. For the purposes of this work, those samples serve as controls for the samples obtained by emulsion polymerization.

Sample names (**W-E-xx-yy, W-H-xx-yy, S-E-xx-yy, and S-H-xx-yy**) designate the preparation route, **W-** for emulsions (water), **S-** for solvent (toluene), the cross-linker, **E-** for EGDMA, **H-** for HDDA, and define the limits of the AN:(AN+cross-linker) v/v ratio, **xx**, and of the total monomers:solvent v/v ratio, **yy**. Outside those limits, gels were either too weak or too dense and of no further interest. Qualitatively, there is an inverse relationship between sample robustness and the relative amount of AN. For instance, if the AN:(AN+cross-linker) v/v ratio is increased above 0.75, samples become too weak.

Scheme 2 summarizes the two synthetic routes to PAN aerogels and includes carbonization and graphitization (see Sections 3.d.1 and 3.d.2). Gelation was induced photochemically at room temperature by irradiation for 300 s. Wet-gels were aged at slightly elevated temperatures. Prompted by a reviewer comment, samples of a representative formulation (**W-H-50-40**) were irradiated for 300 s, 600 s, 20 min, 40 min, and 1 h and processed further with no postgelation heat treatment. Upon characterization (Table S.1 in the Supporting Information) it was found that 300 s of irradiation was enough

dx.doi.org/10.1021/cm202975p | *Chem. Mater.* 2012, 24, 26−47

Scheme 2. Solution (S-) and Emulsion (W-) Polymerization Routes to Polyacrylonitrile (PAN) Aerogels Followed by Carbonization and Graphitization

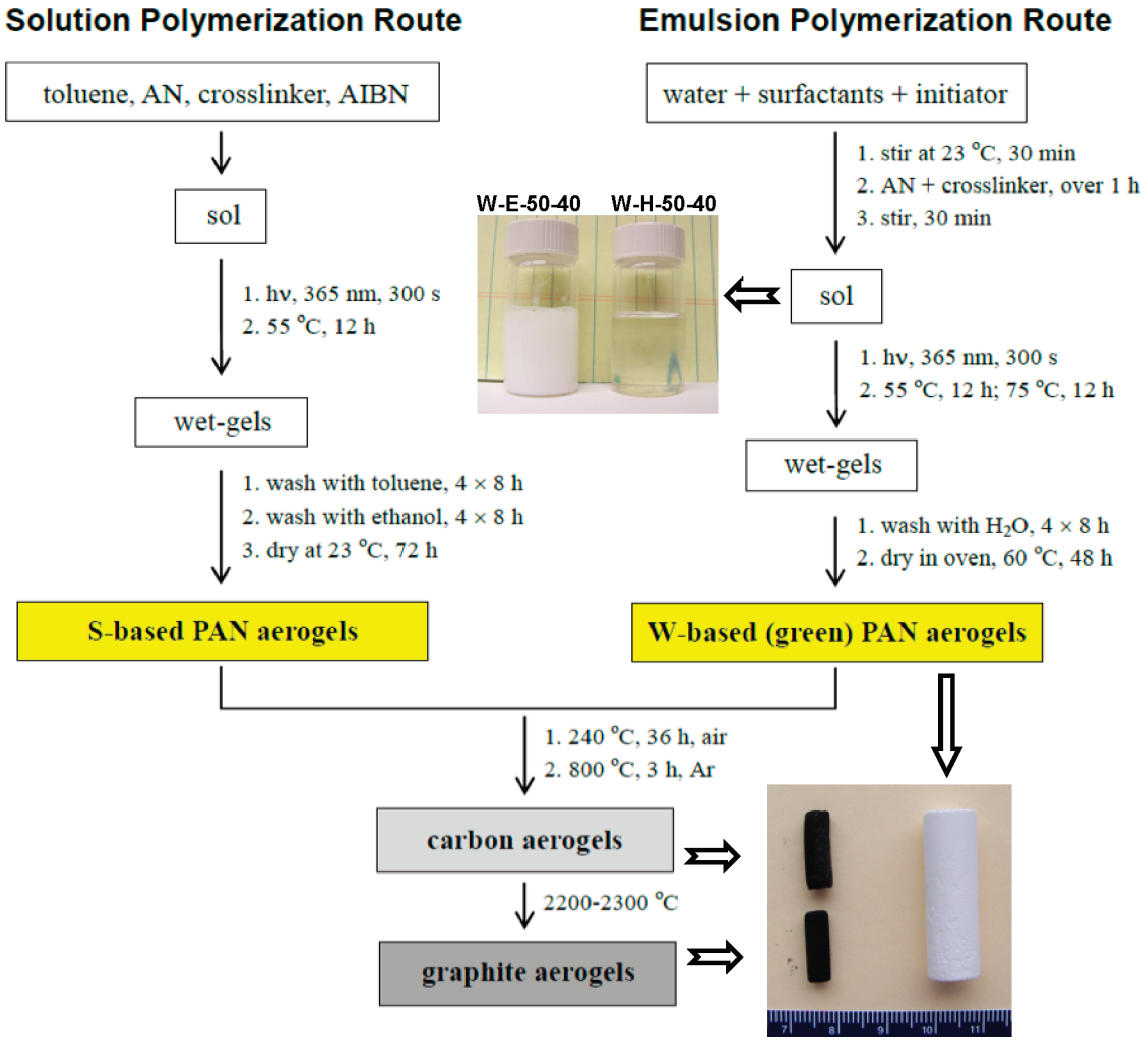

to reach terminal properties, thus rendering all aging completely unnecessary. Washes from either route were analyzed (by GC) for unreacted monomers. None was detected, meaning that all monomers were incorporated in the gels. Wet-gels were dried with SCF CO_2 as well as under ambient pressure, and again they were found to have identical properties (see Table S.2 in the Supporting Information). All subsequent discussion is based on materials dried under ambient pressure.

3.b. Characterization of the Emulsions and the Sol–Gel Transition. The primary concern in formulating our emulsions was not optical clarity but rather stability during the 300 s of photogelation. ("Stability" in the sense that emulsions would not separate into layers or form flocs.) For the most part that was accomplished by combining cationic ***surf-1*** and nonionic Triton X-100. It is known that ionic surfactants (soaps) form micelles that can be swollen only within narrow limits by monomers; most monomers then stay out of the micelles forming droplets in the 1−10 μm size regime, hence those (macro)emulsions scatter light and are opaque (milky).[43] High soap concentrations in combination with nonionic amphiphilic stabilizers (in this case Triton X-100) form mixed micelles that can expand with monomers indefinitely, yielding microemulsions, which are clear as the diameter of the droplets (typically <100 nm) is less than a quarter of the wavelength of the visible light.[43] In our case, the sole exception in that scheme was **W-E-50-40**, which, in its initial formulation with ***surf-1***/Triton X-100, was neither clear nor photostable. Eventually, it became photostable by replacing ***surf-1*** with anionic SDS (Table 1), albeit it remained opaque-white (see photograph in Scheme 2) and quasi-stable, meaning that it would separate into two layers upon standing for a few hours. Finally, prompted by the milky appearance of **W-E-50-40**, and for control purposes (see below), we introduced an extra sample, **W-H-75-50***, even though the original **W-H-75-50** was already photochemically stable (and clear). **W-H-75-50*** was made by replacing ***surf-1*** with SDS, and it was quasi-stable/milky (Table 1).

EGDMA and HDDA by themselves are not soluble in water (confirmed by refractive index measurements). With no surfactants, all formulations are two-phase systems (Figure 1A-a). On the other hand, owing to the finite solubility of AN in water (~7% w/w at room temperature), 7−13% w/w of AN in the formulations considered may be extracted by the aqueous layer (Figure 1B). Being a surfactant itself, ***surf-AIBN*** is expected to form a monolayer around large monomer droplets (leaving the anionic initiator in the aqueous phase). Indeed, addition of only ***surf-AIBN*** creates a milky (macro)emulsion (Figure 1A-b) that settles in a few hours (Figure 1A-c). Those emulsions are used in control experiments described below in order to investigate

dx.doi.org/10.1021/cm202975p | *Chem. Mater.* 2012, 24, 26–47

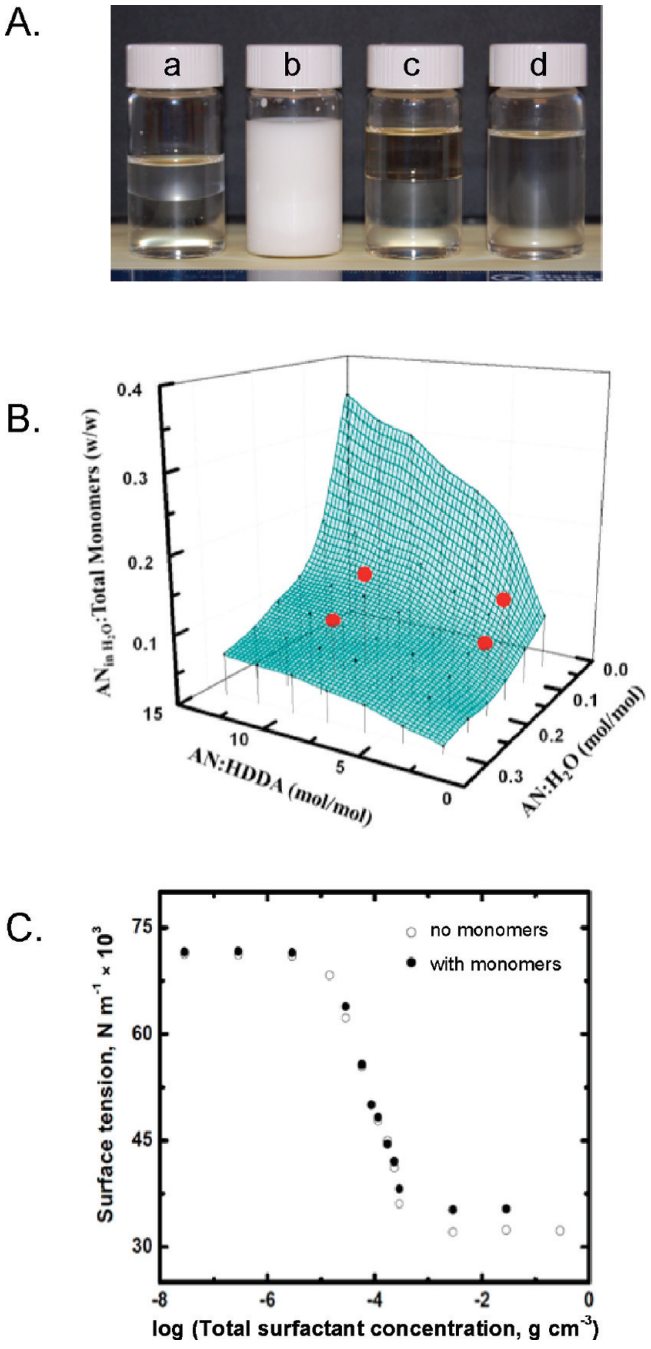

Figure 1. A. The **W-H-50-40** formulation without surfactants forms a two-phase system (a); upon addition of only ***surf-AIBN*** it forms a milky, quasi-stable emulsion (b), which settles after a few hours into a two-phase system (c); upon addition of all surfactants (see Table 1) it gives a clear, indefinitely stable emulsion (d). B. Weight fraction of AN in the aqueous phase of two-phase systems (no surfactants) as a function of AN:HDDA and AN:water mol fractions. Red dots correspond to the formulations used to make emulsions (Table 1). C. Surface tension versus surfactant concentration with and without monomers. Error bars within the symbols (not visible). Initial composition at right corresponds to the **W-H-50-40** sample. Only one CMC point is identified and remains about the same in both cases: $CMC_{no\_monomers}$ = 0.47 g L^{-1}; $CMC_{with\_monomers}$ = 0.41 g L^{-1}.

possible concurrent solution polymerization in the continuous aqueous phase. Eventually, all surfactants are needed to turn the emulsions clear and stable (Figure 1A-d). With all surfactants present, the surface tension versus surfactant concentration profiles (Figure 1C) remain generally unaffected by the presence of monomers (AN+cross-linker) meaning that the continuous phase is always water. Meanwhile, at 22 °C, the surface tension of water was measured at 72.57 ± 0.02 dyn cm^{-1}, of pure AN at 25.99 ± 0.05 dyn cm^{-1} (lit.: 72.8 dyn cm^{-1} at 20 °C and 27.3 dyn cm^{-1} at 24 °C, respectively), and of AN-saturated water at 55.31 ± 0.31 dyn cm^{-1}. At none of its ends the profile of Figure 1C shows the expected signature (in terms of reduced surface tension) of AN dissolved in water. The single Critical Micelle Concentration (CMC; Figure 1C) is in agreement with mixed micelles expected of microemulsions, and the surfactant(s) concentration in the formulations (in the order of 445−520 g L^{-1}) was approximately 1000−4,000× higher than the CMCs. At this point, for further insight into the gelation process, it was deemed necessary to correlate quantitatively the micelle size with the size of the resulting primary particles. That was done with small angle neutron scattering (SANS). Samples for SANS were selected to provide a representative cross-section of the synthetic parameters.

Typical SANS data are represented in Figure 2 by the clear-stable emulsion **W-H-75-50**, its quasi-stable milky counterpart **W-H-75-50*** and the corresponding aerogels. Figure 2 also includes the SANS data for the **S-H-75-50** aerogel, prepared by solution polymerization in toluene. Data for all samples tested are summarized in Table 3. Emulsion data were obtained at three different temperatures. With the exception of the **W-E-75-50** emulsion, clearly defined peaks are observed in all other emulsion data, indicative of liquid-like order. Based upon their breath, it is concluded that the peaks define characteristic length scales of the emulsion rather than Bragg scattering. The peak positions are not affected by the temperature up to 40−45 °C. Afterward, the scattering profile of all clear emulsions (e.g., of **W-H-75-50**) changes shape, with the peak position shifting to higher *Q*-values, and a new power-law region shows up at low-*Q*s. The latter might be attributed either to onset of polymerization and formation of aggregates (secondary particles) or to changes in the structure of the emulsion, for instance by breaking-up of mixed micelles into e.g., two types of micelles, one for each surfactant. We are inclined toward the second interpretation as both types of emulsions (clear and milky) should have the same onset of thermal polymerization, hence they should have evolved similarly. (It is noted that CMC determination at elevated temperatures was not experimentally accessible.) Aerogels, on the other hand, show a power-law region at high *Q*s, followed by a Guinier knee, most likely corresponding to the radius of gyration, R_G, of the primary particles. Probing larger aggregates was outside our experimentally accessible range at low *Q*s.

Quantitative analysis of the emulsion data was conducted according to a model that assumes micelles to be spheroids of revolution with an average radius R_s and with a hard sphere-like interaction potential at distance *D* from the sphere center.[44] For that so-called fluid model, the entire differential cross-section per unit volume, $I(Q)$, versus *Q* data (Figure 2) are fitted according to eq 2, where $P(R_s,Q)$ is the form factor

$$I(Q) = I_o \cdot P(R_s, Q) \cdot S(D, \Phi, Q) \quad (2)$$

for a spherical micelle of radius R_s, $S(D,\Phi,Q)$ is the structure factor, describing the micelle interactions and is calculated assuming hard-sphere interactions for the micelles using the Percus−Yevick model and gives the hard sphere interaction radius, *D*;[45] Φ is the volume fraction of the micelles, and I_o is the scaling parameter related to the details of the micelle structure.

dx.doi.org/10.1021/cm202975p | *Chem. Mater.* 2012, 24, 26−47

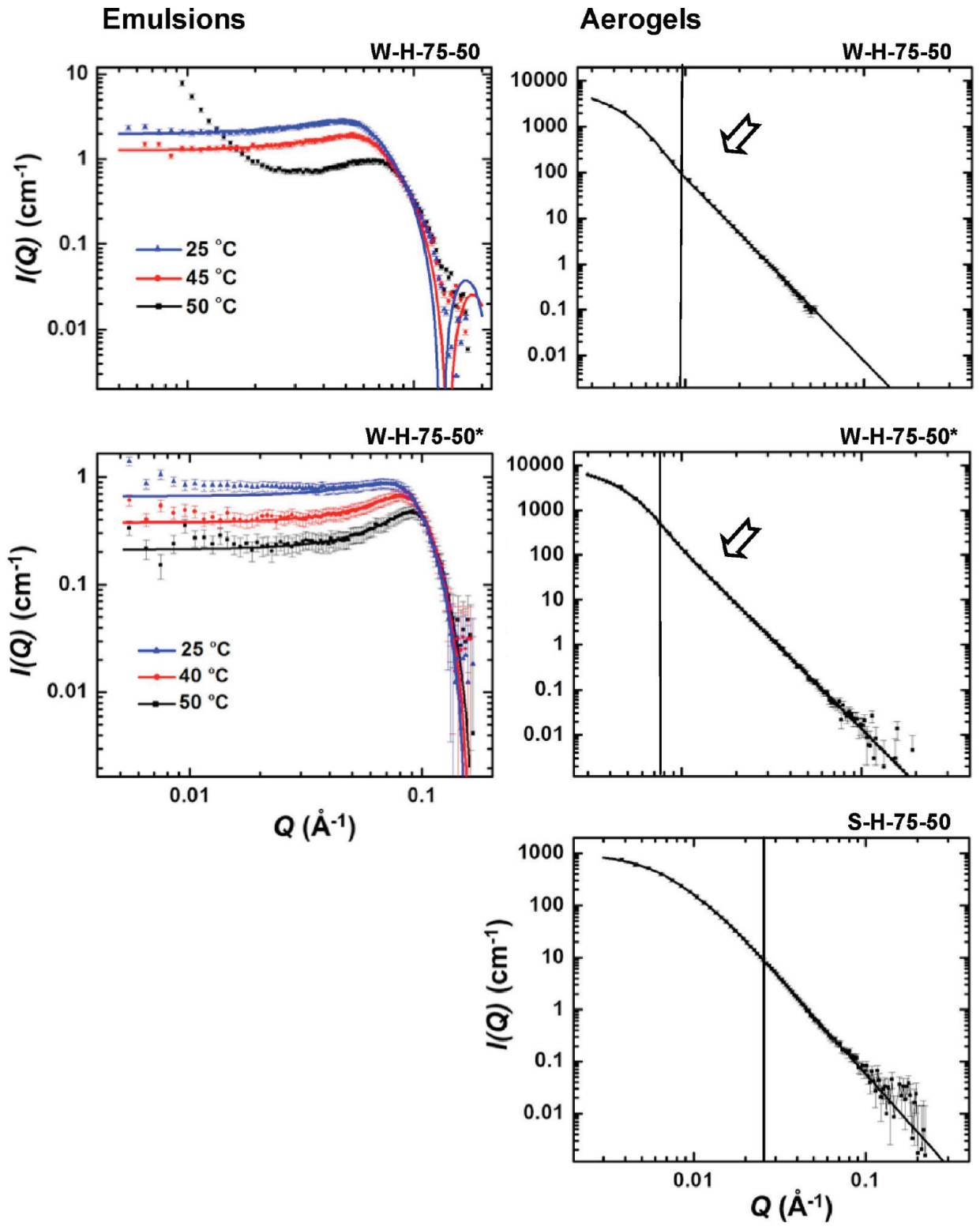

Figure 2. SANS data of representative emulsions and the corresponding aerogels. **W-H-75-50**: clear/stable emulsion, **W-H-75-50***: milky/quasi-stable emulsion. **S-H-75-50** sample prepared from solution polymerization in toluene. Data for emulsions have been obtained at three different temperatures and have been fitted assuming liquid-like order of spherical micelles. Vertical lines separate the high-Q power-law region from the Guinier knee. Arrows indicate the minor deflections that suggest multiple scattering (see text).

According to this model, micelles cannot have a center-to-center distance of less than $2D$. Both the R_s and D are cited in Table 3. The numerical proximity of R_s and D suggests that for the surfactant volume fractions employed, the solutions are practically filled with micelles. Meanwhile, the molecular length of fully extended ***surf-1*** is 1.52 nm (by modeling) and not larger than 0.8 nm in diameter in the fully coiled form. Since R_s is on average double than the length of the fully extended surfactant, it is concluded that micelles contain a significant portion of the monomer.

dx.doi.org/10.1021/cm202975p | *Chem. Mater.* 2012, 24, 26–47

Table 3. SANS Data for Selected Emulsions and the Corresponding Aerogels

	emulsion (25 °C)		aerogel		
sample	R_s (nm)	D (nm)	high-Q slope	R_G (nm)	R (nm)[a]
W-E-75-50	3.03 ± 0.05	–	3.45 ± 0.02	44.4 ± 1.2[b]	57.7[b]
W-H-50-40	2.88 ± 0.06	3.52 ± 0.06	4.00 ± 0.05	43.0 ± 1.1[b]	55.8[b]
W-H-75-50	3.39 ± 0.04	4.55 ± 0.05	4.00 ± 0.05	45.4 ± 1.4[b]	59.0[b]
W-H-75-50*	2.88 ± 0.08	3.1 ± 0.1	4.00 ± 0.04	42.6 ± 1.1[b]	55.3[b]
S-H-75-50			3.64 ± 0.02	26.4 ± 1.4	34.0

[a]Radius, R, calculated via $R_G = 0.77 \times R$. [b]Possible multiple scattering.

Table 4. Selected Properties of Emulsion (Water)-Based PAN Aerogels

sample	[monomers] in sol (M)	linear shrinkage (%)[a,b]	bulk density, ρ_b (g cm^{-3})[a]	skeletal density, ρ_s (g cm^{-3})[c]	porosity, Π (%void space)	BET surface area, σ (m^2 g^{-1})	average pore diameter (nm)[d]	BJH plot maxima (nm) [half width (nm)][e]	particle radius, r (nm)[f]
W-E-50-40	3.26	12	$0.40_3 \pm 0.01_4$	1.289 ± 0.005	68	27	20 [253]	29.5 [8.2]	86.2
W-E-50-40-A[g]	3.26	10	$0.43_3 \pm 0.01_8$	$1.23_4 \pm 0.01_1$	64	7	95 [857]	101 [88]	347
W-E-50-50	4.09	4	$0.53_4 \pm 0.01_4$	1.184 ± 0.002	54	35	18 [117]	41.6 [24.4]	72.4
W-E-75-40	4.06	14	$0.38_7 \pm 0.01_1$	1.266 ± 0.004	69	25	23 [287]	36.9 [28.3]	94.8
W-E-75-50	5.06	10	$0.51_2 \pm 0.02_7$	1.174 ± 0.001	56	39	14 [113]	36.3 [12.7]	65.5
W-H-50-40	3.12	10	$0.43_2 \pm 0.03_7$	1.215 ± 0.002	64	27	24 [221]	27.5 [15.9]	91.4
W-H-50-40-A[g]	3.12	9	$0.44_2 \pm 0.04_4$	1.258 ± 0.008	65	9	76 [652]	96.6 [81.6]	265
W-H-50-50	3.90	9	$0.51_5 \pm 0.01_1$	1.175 ± 0.001	56	40	27 [109]	41.6 [42.1]	63.8
W-H-75-40	3.98	12	$0.38_5 \pm 0.01_2$	1.232 ± 0.001	69	26	21 [275]	36.3 [34.9]	93.7
W-H-75-50	4.98	11	$0.52_2 \pm 0.01_1$	1.174 ± 0.001	55	34	18 [125]	37.1 [25.1]	75.2
W-H-75-50*[h]	5.97	10	$0.54_4 \pm 0.03_1$	1.201 ± 0.002	56	31	21 [130]	44.0 [37.8]	80.6

[a]Average of 5 samples. [b]Relative to the molds (1.00 cm diameter). [c]One sample, average of 50 measurements. [d]By the $4 \times V_{Total}/\sigma$ method. For the first number, V_{Total} was calculated by the single-point adsorption method; for the number in brackets, V_{Total} was calculated via $V_{Total} = (1/\rho_b)-(1/\rho_s)$. [e]From the desorption branch of the isotherms. First numbers are the peak maxima; numbers in brackets are the full widths at half maxima. [f]Calculated via $r = 3/\rho_s\sigma$. [g]Samples made using AIBN as initiator (enforcing suspension polymerization). [h]See footnotes *a* and *c*, Table 1.

Table 5. Properties of Selected Solvent (Toluene)-Based PAN Aerogels

sample	[monomers] in sol (M)	linear shrinkage (%)[a,b]	bulk density, ρ_b (g cm^{-3})[a]	skeletal density, ρ_s (g cm^{-3})[c]	porosity, Π (%void space)	BET surface area, σ (m^2 g^{-1})	average pore diameter (nm)[d]	particle radius, r (nm)[e]
S-E-50-40	4.10	3	0.509 ± 0.008	1.273 ± 0.002	60	135	17.2 [34.9]	17.5
S-E-50-50	5.15	2	0.594 ± 0.004	1.290 ± 0.001	53	121	18.1 [30.0]	19.2
S-E-75-40	5.15	1	0.492 ± 0.009	1.258 ± 0.004	69	145	16.6 [34.1]	16.4
S-E-75-50	6.35	1	0.597 ± 0.001	1.263 ± 0.001	59	157	14.1 [22.5]	15.1
S-H-50-40	3.95	8	$0.48_7 \pm 0.02_7$	1.273 ± 0.001	61	42	19.2 [121]	56.1
S-H-50-50	4.90	10	$0.60_5 \pm 0.01_0$	1.219 ± 0.007	47	34	25.1 [97.9]	72.4
S-H-75-40	5.05	5	$0.45_2 \pm 0.03_8$	1.197 ± 0.002	62	56	19.8 [98.4]	44.8
S-H-75-50	6.25	7	$0.56_7 \pm 0.04_9$	1.233 ± 0.003	54	52	17.3 [73.3]	46.8

[a]Average of 5 samples. [b]Relative to the molds (1.00 cm diameter). [c]One sample, average of 50 measurements. [d]By the $4 \times V_{Total}/\sigma$ method. For the first number, V_{Total} was calculated by the single-point adsorption method; for the number in brackets, V_{Total} was calculated via $V_{Total} = (1/\rho_b)-(1/\rho_s)$. [e]Calculated via $r = 3/\rho_s\sigma$.

The scattering profiles of the corresponding aerogels were fitted with the Beaucage Unified Model[46] as described for other organic aerogels recently.[8,10b,47] While the scattering profile of the **S-H-75-50** aerogel is smooth throughout, all **W**-aerogels uniformly show minor deflections at $Q \sim 0.01$ Å^{-1} (pointed by arrows) suggesting possible multiple scattering, meaning that neutrons may have scattered more than once before exiting the sample. The end result is that the R_G values reported are likely smaller than their true values; however, the high-Q slopes are unaffected. Additional experimental effort would be required to completely understand the possible multiple scattering effects[48] and falls outside the scope of this work.

Irrespective of whether emulsions were clear/stable (e.g., **W-E-75-50**, **W-H-50-40**, **W-H-75-50**) or quasi-stable/milky (e.g., **W-H-75-50***) SANS analysis yields much larger primary particles (radii in the range of 55−59 nm) than the original micelles (radii in the range of 2.9−4.6 nm). Interestingly, even solution polymerization yields unusually large primary particles (34 nm in radius, sample **S-H-75-50**). At this point, it is also noted that the primary particle sizes of all aerogels for which SANS data are available (R values in Table 3) are in the same range with particle sizes (r values in Tables 4 and 5) calculated from skeletal densities, ρ_s, and BET surface areas, σ, via $r = 3/\rho_s\sigma$. Therefore, particle radii, r, calculated by the latter method

dx.doi.org/10.1021/cm202975p | *Chem. Mater.* 2012, 24, 26−47

are considered reliable, and in that regard Table 4 shows that all emulsions, clear/stable or quasi-stable/milky, yield aerogels with particle radii in the same range, again much larger than the micelles in their sols (Table 3). Overall, comparison of micelle and primary particle sizes supports a typical emulsion polymerization model whereas polymerization is initiated in some micelles, which grow into particles by supply of monomers either from larger reservoir droplets, or in this case from similar size micelles, via short diffusion through water.[33] If reservoir droplets do exist, their presence is inferred only by the relative micelle and primary particle sizes, as they fall beyond the experimentally accessible range of our SANS (<100 nm).

The presence of larger reservoir droplets was investigated further by varying the location of the initiator. For this, we conducted control experiments whereas instead of ***surf-AIBN***, polymerization was induced with either the triethylammonium salt of 4,4′-azobis-(4-cyanovaleric acid), ***sol-AIBN***, or AIBN itself. ***Sol-AIBN*** is water-soluble, and in all aspects a typical emulsion polymerization initiator. ***Surf-AIBN*** shares the same amphiphilic cation with the main surfactant, ***surf-1***, and should be associated closely with the micelles. AIBN on the other hand is lipophilic, soluble in the monomer reservoir droplets, and should trigger formation of larger particles as in a suspension polymerization-like process. (The logic followed here is akin to the recent use of inverse suspension polymerization of an emulsified RF aqueous solution for the synthesis of carbon aerogel spheres.[35]) Materials obtained with ***sol-AIBN*** (data not shown) are strictly identical to those with ***surf-AIBN*** suggesting that ***surf-AIBN*** does not partition inside monomer droplets (if they exist), thus excluding the possibility for concurrent suspension polymerization. That argument becomes stronger if we deliberately induce polymerization in the reservoir droplets. For this, two aerogels, **W-E-50-40-A** and **W-H-50-40-A**, obtained with AIBN instead of ***surf-AIBN*** (refer to Table 4), have significantly lower surface areas, much larger pore diameters, and on average they consist of much larger particles (265−347 nm in radius, by the $r = 3/\rho_s\sigma$ method) than aerogels **W-E-50-40** and **W-H-50-40** obtained from the same emulsions with water-soluble ***surf-AIBN*** (particle radii 64−95 nm). Upon closer examination yet, particle sizes from milky **W-E-50-40-A** are larger (347 nm) than particle sizes from clear **W-H-50-40-A** (265 nm), consistent with a macro versus a micro character for those emulsions.

Both SANS and location-of-initiator experiments point toward gelation via a mechanism that is consistent with classical emulsion polymerization.[33] To investigate the possibility of concurrent emulsion and solution polymerization (owing to the finite solubility of AN in water), we irradiated and heated solutions in which ***surf-AIBN*** (in its typical concentration − see Table 1) played the dual role of initiator and surfactant (i.e., the samples shown in Figure 1A-b). The microstructure of the resulting solids is distinctly different from what is obtained by the regular process with all surfactants present, consisting of two kinds of very large particles (about 0.5 and 4 μm, see Figure S.1 in the Supporting Information), consistent with concurrent solution polymerization of soluble AN, and surface-initiated suspension polymerization of ***surf-AIBN***-stabilized large monomer droplets. As we shall see below, this kind of microstructure is not visible in any of our samples. Therefore, although concurrent solution polymerization may be conceivable, we do not expect (based on the results of Figure 1C) and we see no SEM evidence in the regular formulations.

3.c. Characterization of PAN Aerogels. General material properties of **W**- and **S**-type samples are summarized in Tables 4 and 5, respectively. Table 4 includes the entire domain of **W**-samples (plus controls as discussed in Section 3.b). For direct comparison, Table 5 shows only samples corresponding to those of Table 4. (For the entire domain of the **S**-samples refer to Table S.3 in the Supporting Information.) Data in the two tables have been grouped to emphasize major trends irrespective of processing (**W**- vs **S**-), which, as discussed below, are traced only to the chemical identity of the cross-linker, EGDMA or HDDA.

By solids ^{13}C NMR (Figure 3), PAN aerogels by both the solution and emulsion polymerization methods incorporate all

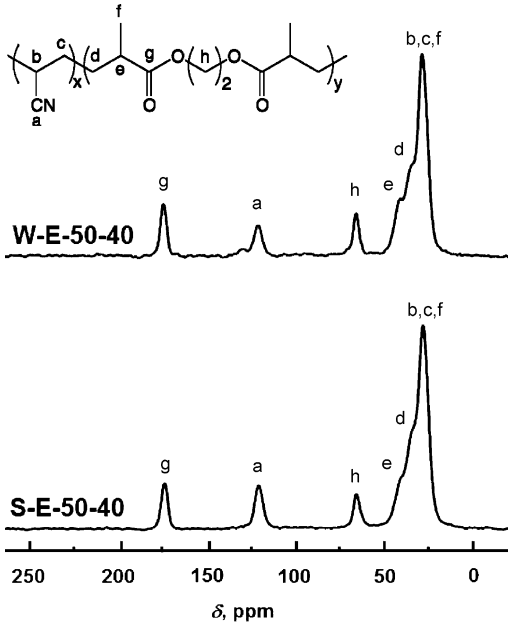

Figure 3. Solids ^{13}C CPMAS NMR data of two PAN aerogels, one made by emulsion polymerization in water (**W**-) and a similar one made in toluene (**S**-). The polymer structure is a simplification for the purpose of resonance assignment.

features of the monomers: C=O at 174−175 ppm, CN at 121 ppm, $COOCH_2$ at 64−65 ppm, and aliphatic carbons in the 25−50 ppm range. **W**-aerogels are free of surfactants: their CHN analysis is within error equal to that of the **S**-samples (Table S.4), and also because no ^{13}C NMR resonance could be associated with the surfactants (for the ^{13}C NMR of ***surf-1*** see the Experimental Section).

Skeletal densities, ρ_s, of all PAN aerogels fall in the 1.2−1.3 g cm^{-3} range, close to that of pure PAN (1.17−1.22 g cm^{-3}, most commonly at 1.18 g cm^{-3}),[49] and the difference is attributed to the cross-linkers. Bulk densities, ρ_b, are significantly lower than ρ_s (in the range 0.385−0.597 g cm^{-3}). It is also noted that **W**-aerogels are less dense (by 14 ± 4%) than their **S**-counterparts. That mostly reflects the lower molar monomer concentrations of the **W**-sols (by ∼21%, see Tables 4 and 5), which are partially offset by the higher linear shrinkage of the **W**-(9−14%) versus the **S**-aerogels (1−10%). (Indeed, by normalizing the molar monomer concentrations by [1-(% linear shrinkage/100)]^3, we obtain **S**-/**W**- concentration ratios similar to those obtained by dividing the corresponding ρ_b values.) Porosities, Π, are calculated from the ρ_b and ρ_s values (see the

dx.doi.org/10.1021/cm202975p | *Chem. Mater.* 2012, 24, 26−47

Table 6. Mechanical Properties under Quasi-Static Compression of PAN Aerogels

sample	bulk density ρ_b, (g cm^{-3})	strain rate (s^{-1})	Young's modulus (E, MPa)	speed of sound (m s^{-1})[a]	ultimate compressive strength (MPa)	ultimate strain (%)	specific energy absorption (J g^{-1})
Emulsion Based (**W-**) Aerogels							
W-E-50-40	$0.40_3 \pm 0.01_4$	0.005	2.1 ± 0.3	73.7	0.52 ± 0.05	23 ± 3	$0.14_6 \pm 0.01_2$
W-E-50-50	$0.53_4 \pm 0.01_4$	0.005	9.4 ± 0.8	152.0	1.36 ± 0.05	14 ± 1	0.237 ± 0.008
W-E-75-40	$0.38_7 \pm 0.01_1$	0.005	4.1 ± 0.5	106.3	$0.9_1 \pm 0.1_0$	20 ± 2	$0.17_1 \pm 0.01_9$
W-E-75-50	$0.51_2 \pm 0.02_7$	0.005	22 ± 3	238.4	1.25 ± 0.05	9 ± 1	$0.14_2 \pm 0.02_7$
W-H-50-40	$0.43_2 \pm 0.03_7$	0.005	$4._8 \pm 1._1$	111.3	0.53 ± 0.04	37 ± 3	$0.26_5 \pm 0.03_8$
W-H-50-50	$0.51_5 \pm 0.01_1$	0.005	3.6 ± 0.9	94.6	$0.8_1 \pm 0.1_8$	22 ± 2	$0.20_4 \pm 0.04_3$
W-H-75-40	$0.38_5 \pm 0.01_2$	0.005	2.4 ± 0.8	81.4	0.19 ± 0.03	20 ± 2	0.038 ± 0.007
W-H-75-50	$0.52_2 \pm 0.01_1$	0.005	30 ± 5	273.8	1.93 ± 0.02	7 ± $0._1$	$0.27_8 \pm 0.01_9$
Solvent Based (**S-**) Aerogels[b]							
S-E-50-40	0.509 ± 0.008	0.01	134 ± 3	258	21 ± 2	63 ± 3	$3._8 \pm 1._2$
S-E-50-50	0.594 ± 0.004	0.01	246 ± 14	644	68 ± 13	67 ± 2	18 ± 2
S-E-75-40	0.492 ± 0.009	0.01	17 ± 2	186	7 ± 3	61 ± 2	1.2 ± 0.4
S-E-75-50	0.597 ± 0.001	0.01	175 ± 22	588	95 ± 7	64 ± 3	12 ± 4
S-H-50-40	$0.48_7 \pm 0.02_7$	0.01	102 ± 9	458	11 ± 3	58 ± 4	12 ± 3
S-H-50-50	$0.60_5 \pm 0.01_0$	0.01	191 ± 17	562	110 ± 13	52 ± 4	17 ± 2

[a]Calculated by: speed of sound = $(E/\rho_b)^{0.5}$. [b]Samples **S-H-75-40** and **S-H-75-50** from Tables 2 and 5 were too weak and were not tested.

Experimental Section) and fall in the 47−75% v/v range (Tables 4 and 5).

All shrinkage in the **W**-samples takes place during drying, and it is in the same range, 9−14%, irrespective of cross-linker, **E**- or **H**-. The shrinkage of the **S**-samples takes place during the 300 s of photogelation. Importantly, **S-H**-samples shrink more (5−10%) than the **S-E**-samples (1−3%, only). Considering the surface tension of water and toluene at 20 °C, 0.0720 N m^{-1} and 0.0284 N m^{-1}, respectively, those data could support that **W**-samples shrink more because of the higher surface tension forces of evaporating water, whereas **S**-samples can tolerate the lower surface tension of evaporating toluene better. However, this explanation is *not* consistent with the data of Table S.2 showing that **W**-samples dried either under ambient pressure from water or with SCF-CO_2 are practically indistinguishable. Therefore, **W**- and **S**-samples tolerate their evaporating solvents equally well, hence shrinkage in both cases is rather associated with the usual osmotic effects causing polymer swelling:[23b] in the case of **S**-samples a developing strong network pulls itself together while it is being formed causing expulsion of solvent (syneresis), whereas in the case of the **W**-samples a less rigid framework (see evidence below via mechanical characterization) causes no syneresis and deswells later by loss of solvent during drying. Within that model, the higher shrinkage in **S-H**- samples is attributed to the more flexible molecular structure of HDDA, while in the **S-E**-samples EGDMA plays more the role of a rigid spacer. (The different flexibilities of the two cross-linkers are reflected to and are supported by the heat capacities of the corresponding aerogels, which at 25 °C are 1.3−1.4 J g^{-1} K^{-1} for the **H**-samples, versus 1.1−1.2 J g^{-1} K^{-1} for their **E**-counterparts; see Table S.5 in the Supporting Information.)

However, irrespective of the factors that cause shrinkage, the key fact is that both **W**- and **S**-wet-gels can be dried under ambient pressure. The absence of collapse into xerogels could be attributed either to (a) an extremely strong skeletal framework, as in polymer-cross-linked silica aerogels,[50] or to (b) large pores, whereas the pressure difference exerted on the pore walls across the liquid−vapor interface, being inversely proportional to the pore radius, would be greatly reduced relative to that in typical mesoporous aerogels.[34a] With regards to the first possibility, the mechanical properties of the **W**- and **S**-aerogels were characterized by quasi-static compression, and the results are reported in Table 6. (Typical data are shown in Figure S.2 in the Supporting Information.) **S**-samples are overall much stiffer than the emulsion-based **W**-samples (Young's modulii in the ranges of 17−246 MPa vs 2−30 MPa, respectively), and they fail at much higher stresses (up to 110 MPa vs 0.52−1.93 MPa for the **W**-samples) and strains (52−63% versus 7−23%, respectively).[51] The vast difference in the mechanical properties between **W**- and **S**-aerogels suggests that the layer of the surfactant prevents intimate contact and efficient covalent bridging between the skeletal nanoparticles. Overall, our ability to dry **W**- or **S**- monoliths under ambient pressure cannot be attributed to the mechanical properties of the framework. Therefore, the next step was to investigate the morphology of the porous structure by SEM and N_2-sorption porosimetry.

Figure 4 shows the microstructures and the N_2-sorption isotherms of two representative **W**-aerogel samples, one from a clear and one from a milky emulsion (**W-E-50-50** and **W-E-50-40**, respectively), as well as the data from the corresponding **S**-aerogel (**S-E-50-40**), and from a typical **H**-sample (**S-H-50-50**). By SEM all samples appear similar. At higher magnifications they all consist of 30−80 nm in diameter globules (indicated by circles) that could be considered as clusters of smaller particles. Despite that appearance, however, both SANS (Table 3) and particle radius calculations from skeletal density and BET surface areas (Tables 4 and 5) indicate that those globules are indeed the smallest building blocks of the material (primary particles). In certain cases, their "bumpy" texture amounts not to finer structure (smaller particles) but instead to surface fractality, as suggested by the slopes of the power-laws at high Qs in SANS, which are between 3.0 and 4.0 (Table 3). Most importantly though, SEM suggests that all samples are macroporous. Indeed, the N_2-sorption isotherms rise above P/P_o = 0.95, do not reach saturation, and show narrow hysteresis loops, both consistent with macroporous materials with some mesoporosity. Average pore diameters calculated by the $4V_{Total}/\sigma$ method, whereas V_{Total} is calculated via $V_{Total} = (1/\rho_b)\text{-}(1/\rho_s)$, are up to 10× larger than the pore diameters calculated with V_{Total} taken from the highest point in the isotherm (see Tables 4 and 5). Actually, the wider the discrepancy in the pore diameters calculated by the two methods,

dx.doi.org/10.1021/cm202975p | *Chem. Mater.* 2012, 24, 26−47

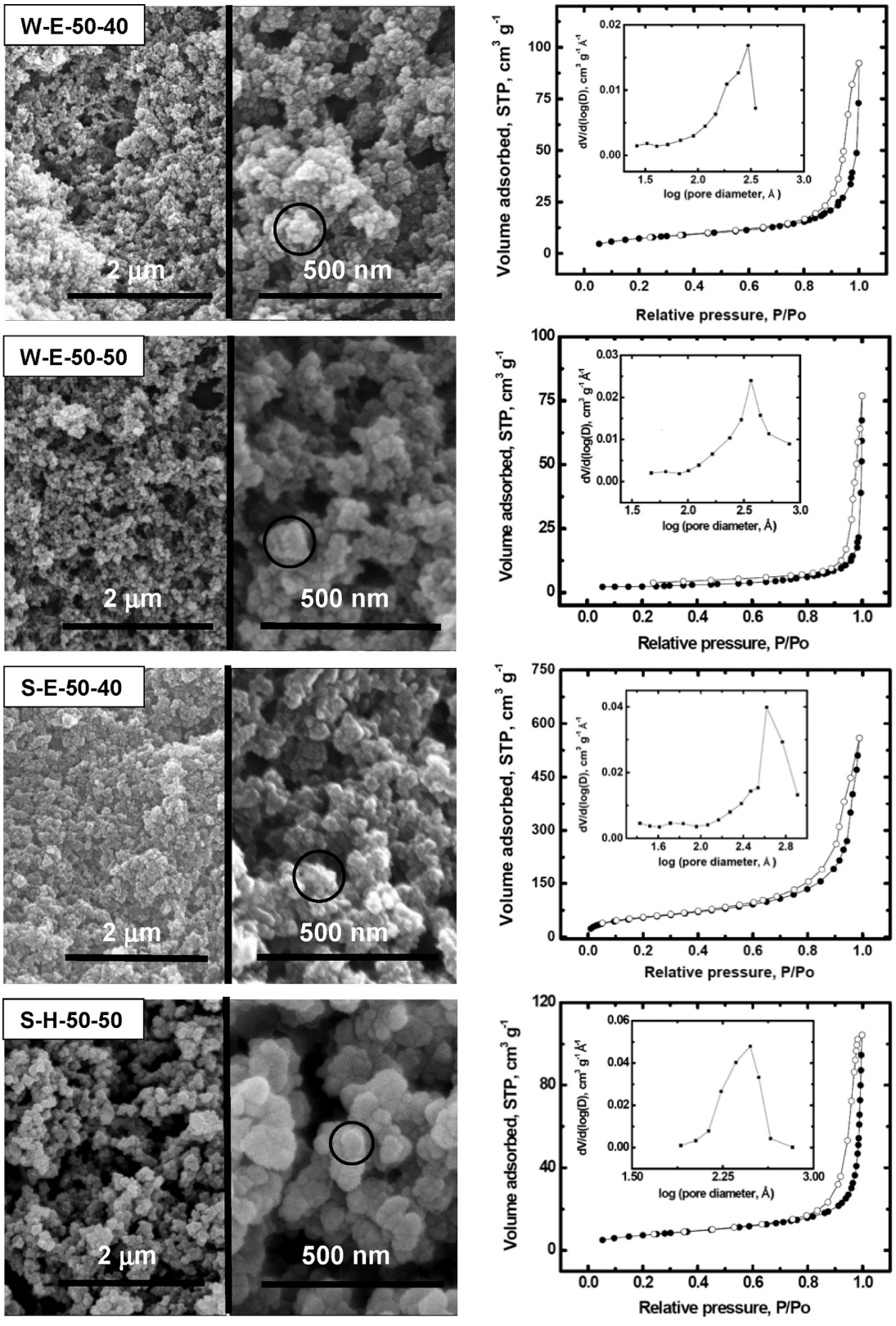

Figure 4. SEM and N_2-sorption data of representative emulsion (**W**-) and solution (**S**-) based PAN aerogels. Insets show the BJH plots derived from the desorption branch of the isotherms. Circles show the fundamental building blocks of the network (see text).

the more of the porosity is attributed to macropores. This is particularly the case with all **W**-samples (Table 4). By the same token, it is also noted that there is generally a better agreement in the average pore diameters calculated by the two methods for the **S**-**E**-samples, suggesting a significant amount of mesopores (see Table 5). Mesopores, presumably formed by the narrow space between the large skeletal nanoparticles, are actually present in all samples, and judging from the shape of the BJH plots (insets in Figure 4), their size distribution is broad and in some cases multimodal. Overall, SEM and N_2-sorption

dx.doi.org/10.1021/cm202975p | *Chem. Mater.* 2012, 24, 26–47

data together confirm that bottom-up PAN aerogels are mostly macroporous materials and provide a reasonable explanation for our ability to dry PAN aerogels under ambient pressure.

Now, the similar skeletal and porous structures of the **W**- and **S**-samples, in spite of their different origin, is intriguing. In **S**-sols, particles phase-separate when the polymer meets its solubility limit. With more flexible HDDA that takes place when particle radii reach 50−70 nm; with more rigid EGDMA that occurs much earlier, that is when particle radii reach only 15−19 nm (Table 5). Larger particles in **S**-**H**-aerogels produce lower surface areas (34−56 $m^2\ g^{-1}$); smaller particles in **S**-**E**-samples yield higher surface areas (121−157 $m^2\ g^{-1}$). In **W**-sols on the other hand, virtual primary particles (micelles) are already phase-separated and grow until all monomer is consumed. That takes place when the particle radii are between 64 and 95 nm, irrespective of cross-linker (Tables 3 and 4). Surface areas are correspondingly low (25−40 $m^2\ g^{-1}$, Table 4). As far as primary particles are concerned, in all cases those are large and thus expected to form large pores (macropores). But most probably, this is not the complete picture yet. As identified by SANS, micelles almost completely fill the solution, so that essentially we have larger monomer droplets (identified by the location-of-initiator experiments) surrounded by nanoreactors (micelles) in close proximity. In analogy to HIPEs or surfactant-templated mesoporous silica cellular foams (MCFs),[36] where macropores are created by large amounts of porogens or "swelling agents" (e.g., 1,3,5-trimethylbenzene), here monomer droplets may play the *dual role* of the reservoir *and* the macropore templating agent. Thus, for **S**-aerogels we find pore diameters in the range of 23−121 nm (bimodal distribution, average for **E**- = 30.4 ± 5.7 nm; average for **H**- = 97.7 ± 19.5 nm), while for the **W**-aerogels we have pore diameters between 109 and 287 nm (random distribution, average = 181 ± 76 nm). The difference in pore diameters between the **W**- and **S**-aerogels is much larger than the relative sizes of the corresponding primary particles, supporting the second role of the monomer reservoir droplets as macropore templating agents.

3.d. Pyrolysis of PAN Aerogels. It is well-established that carbonization of PAN requires prior aromatization by heating in air in the 300 °C range.[52] Carbonized PAN can be graphitized by further heating in the 2000−3000 °C range.[22] In order to identify the role of the cross-linkers, EGDMA or HDDA, if any, in the properties of the terminal materials, chemical and morphological changes were followed throughout that process.

3.d.1. Aromatization of PAN Aerogels. Modulated Differential Scanning Calorimetry (MDSC, Figure 5) under N_2 shows only minor, unidentified, heat exchanges up to 300 °C. In air though, all samples show sharp exotherms above 250 °C, associated with eq 3.[52]

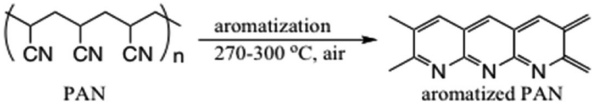

(3)

Aromatized samples are brown, and much more compact (by SEM) than their parent PAN aerogels (Figure 6). Presumably, it is that propensity for contraction that causes samples to break into pieces if heated directly after the exotherm of Figure 5, e.g., at 300 °C. Thus, in order to give samples time to accommodate the structural reorganization imposed by eq 3 and remain monolithic, aromatization was conducted at the foot of the reaction exotherm (at 240 °C). Postaromatization elemental

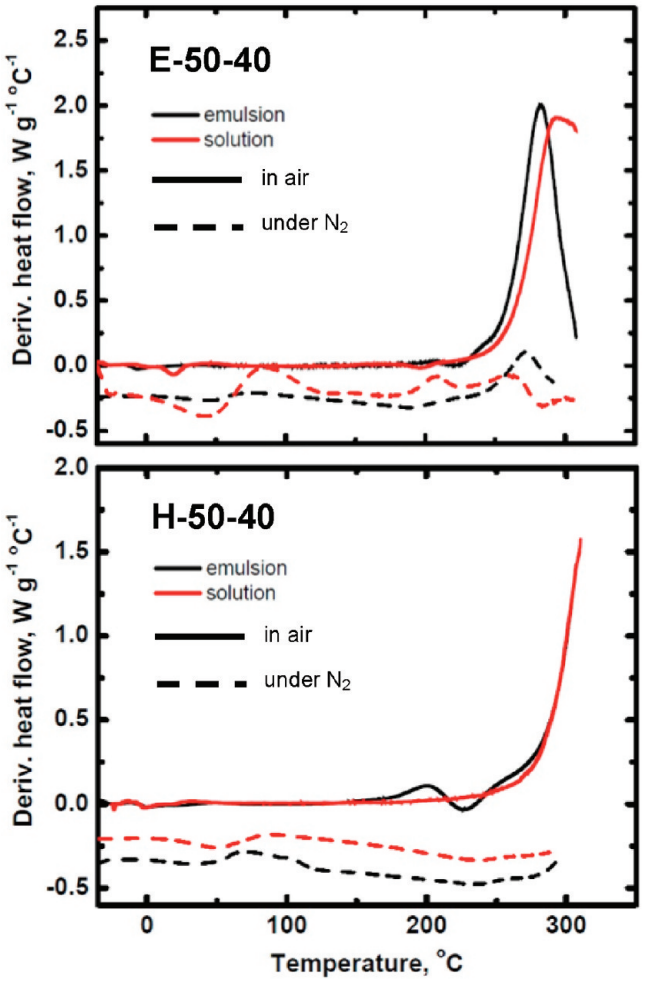

Figure 5. Representative Modulated Scanning Calorimetry (MDSC) data of the samples and conditions shown.

analysis (Table S.4) shows a significant increase in the O content, suggesting a considerable departure from the idealized product of eq 3. Indeed, albeit surviving features from the starting polymers, the ^{13}C NMR spectra of both **E**- and **H**-aerogels show not only resonances assigned (by simulation) to fused pyridines but also to additional carbonyls (Figure 7).[52] Finally, it is important for the following discussion to note that the original **E**-aerogels appear to have a higher crystalline order (by XRD, included in Figure 6), than their **H**-counterparts: although broad, two peaks in the general region of the (100) and the (110) diffractions[53] of the original PAN aerogels are also clearly present in the aromatized sample. It is unclear though whether those diffractions are due to remaining monomer or to the product of eq 3.

3.d.2. Carbonization of Aromatized PAN Aerogels and Materials Properties. Carbonization of aromatized PAN aerogels takes place according to eq 4 and was conducted

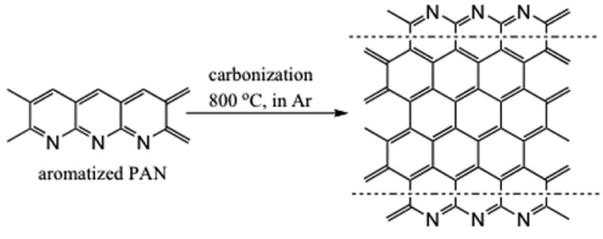

(4)

dx.doi.org/10.1021/cm202975p | Chem. Mater. 2012, 24, 26−47

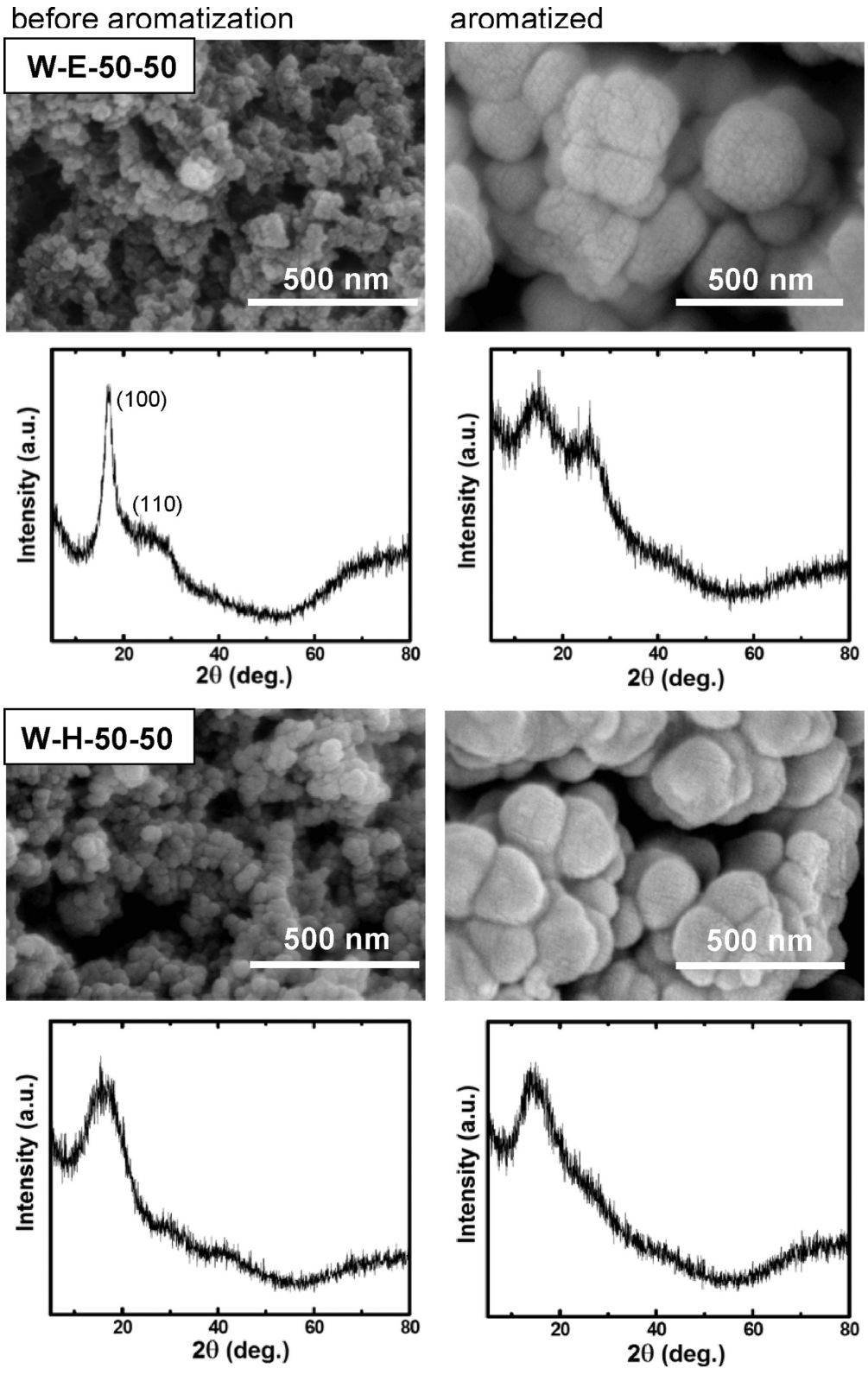

Figure 6. SEM and XRD of two representative samples before and after aromatization. SEM emphasizes the compactness imposed by the contraction expected by eq 3. XRD peak assignments according to ref 53.

under Ar at 800 °C.[22,53] ^{13}C NMR spectra (Figure 7) lose all features associated with the aromatized products. By elemental analysis (Table S.4), we note not only complete loss of H but also relatively high percentages of N and O. The C:N ratio corresponds to a stack of just 3−4 fused rings in the idealized structure of eq 4, and the presence of 8−10% w/w of O suggests a significant amount of defects.

A comprehensive comparison of all material properties of all 800 °C carbons is provided in Table 7. Gravimetric yields (33−57%) are very close to the "theoretical" ones (also included in

dx.doi.org/10.1021/cm202975p | *Chem. Mater.* 2012, 24, 26−47

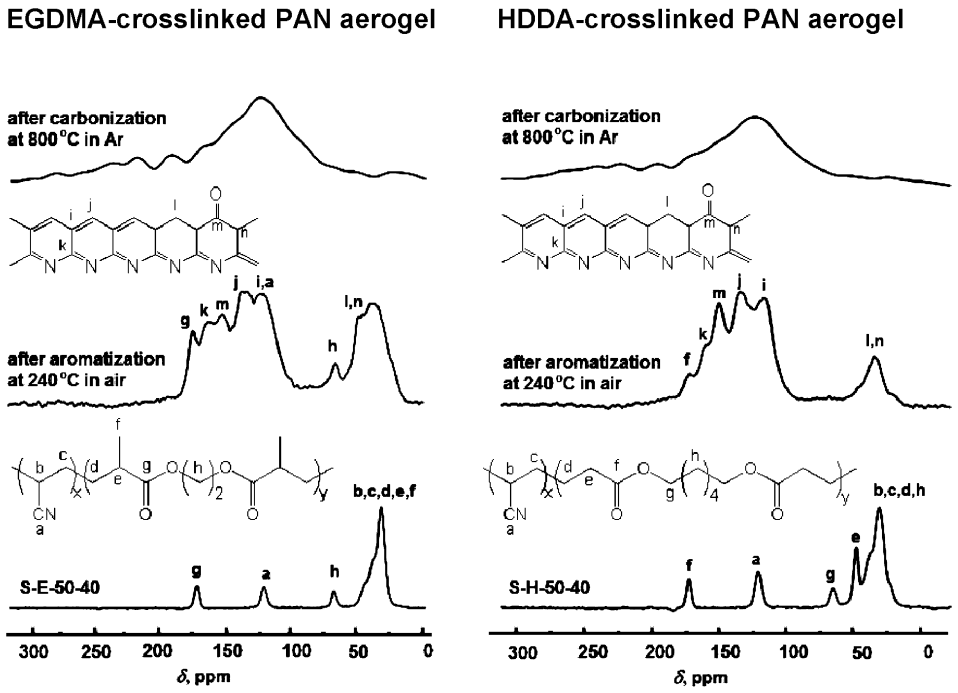

Figure 7. Solids ^{13}C NMR data of two representative PAN aerogel samples showing the changes that accompany aromatization and carbonization after treatment at the temperatures and conditions indicated.

Table 7. Materials Properties of 800 °C Carbon Aerogels, from Emulsion- and Solution Polymerization-Derived PAN Aerogels

sample	% yield (w/w) [theoretical][a]	% linear shrinkage[b]	bulk density, ρ_b (g cm^{-3})[c]	skeletal density, ρ_s (g cm^{-3})[d]	porosity, Π (%void space)	BET surface area, σ (m^2 g^{-1})	average pore diameter (nm)[e]	BJH plot maxima (nm) [half width (nm)][f]	particle radius, r (nm)[g]
Carbons by 800 °C Pyrolysis of Emulsion Based (**W**-) PAN Aerogels									
C-W-E-50-40	37 ± 3 [30.5]	32	$0.57_3 \pm 0.01_1$	1.844 ± 0.002	61	300	18.2 [16.0]	45.7 [30.7]	5.42
C-W-E-50-50	36 ± 2 [30.5]	38	$0.71_3 \pm 0.01_3$	1.834 ± 0.001	68	145	19.1 [23.6]	63.1 [39.3]	11.3
C-W-E-75-40	54 ± 3 [48.9]	43	0.749 ± 0.009	1.920 ± 0.003	67	249	15.1 [13.1]	43.6 [17.4]	6.28
C-W-E-75-50	51 ± 4 [48.9]	43	$0.99_1 \pm 0.01_7$	1.802 ± 0.001	49	137	13.0 [13.3]	24.5 [8.3]	12.2
C-W-H-50-40	34 ± 2 [31.4]	34	0.582 ± 0.008	1.728 ± 0.001	41	43	33.3 [106]	29.5 [20.8]	40.4
C-W-H-50-50	38 ± 4 [31.4]	42	0.632 ± 0.009	1.781 ± 0.001	57	39	35.8 [105]	35.4 [26.5]	43.2
C-W-H-75-40	53 ± 5 [49.6]	33	$0.71_3 \pm 0.01_1$	1.818 ± 0.002	68	42	31.2 [81.2]	29.5 [16.5]	39.3
C-W-H-75-50	51 ± 5 [49.6]	35	$0.92_1 \pm 0.01_8$	1.718 ± 0.003	58	41	28.8 [49.1]	8.9 [4.0]	42.6
Carbons by 800 °C Pyrolysis of Solvent (Toluene) Based (**S**-) PAN Aerogels									
C-S-E-50-40	33 ± 3 [30.5]	35	0.541 ± 0.007	$1.89_3 \pm 0.03_3$	73	204	23.2 [25.9]	31.6 [22.6]	7.77
C-S-E-50-50	37 ± 5 [30.5]	33	0.614 ± 0.009	1.858 ± 0.007	67	183	19.4 [23.8]	36.2 [28.8]	8.82
C-S-E-75-40	52 ± 4 [48.9]	32	$0.69_8 \pm 0.01_5$	1.887 ± 0.009	65	193	14.2 [18.7]	28.2 [19.9]	8.24
C-S-E-75-50	49 ± 2 [48.9]	31	0.815 ± 0.008	$1.81_7 \pm 0.01_2$	57	178	9.4 [15.2]	18.1 [16.2]	9.28
C-S-H-50-40	40 ± 2 [31.4]	57	$0.80_5 \pm 0.01_8$	$1.82_5 \pm 0.03_7$	58	62	28.7 [44.8]	35.5 [27.7]	26.5
C-S-H-50-50	36 ± 4 [31.4]	56	$0.94_5 \pm 0.01_3$	$1.81_9 \pm 0.04_7$	51	46	18.8 [44.2]	25.1 [18.8]	35.9
C-S-H-75-40	57 ± 3 [49.6]	54	$1.04_2 \pm 0.01_9$	$1.89_3 \pm 0.02_3$	45	50	16.3 [34.5]	37.5 [26.6]	31.7
C-S-H-75-50	54 ± 1 [49.6]	53	$1.18_7 \pm 0.02_1$	$1.90_1 \pm 0.01_7$	41	44	18.7 [28.8]	37.2 [24.2]	35.9

[a]Calculated based on the % w/w of AN in total monomers (AN+cross-linker) and a 70% carbonization yield for AN (see text). [b]Relative to the original molds used to make the PAN aerogels (1.00 cm diameter). [c]Average of 5 samples. [d]One sample, average of 50 measurements. [e]By the $4 \times V_{Total}/\sigma$ method. For the first number, V_{Total} was calculated by the single-point adsorption method; for the number in brackets, V_{Total} was calculated via $V_{Total}=(1/\rho_b)-(1/\rho_s)$. [f]From the desorption branch of the isotherm. First numbers are the peak maxima; numbers in brackets are the width at half maxima. [g]Calculated via $r = 3/\rho_s\sigma$.

Table 7), which are calculated based on the following: (a) the literature value of 70% w/w for the conversion yield of PAN to tar at 800 °C[53a,54] and (b) complete loss of all material associated with the cross-linkers. (It is noted that control samples **S-E-00-50** and **S-H-00-50**, made with the cross-linkers alone, see Table S.3 in the Supporting Information, decompose completely by heating at 800 °C under Ar.) Owing to the substantial loss of matter, C-800 °C aerogels shrink significantly (31−57%) relative to their parent PAN aerogels (e.g., see photograph in Scheme 2), but remain monolithic. The combination of mass loss and shrinkage results in bulk densities not very different from those of the starting PAN aerogels

dx.doi.org/10.1021/cm202975p | *Chem. Mater.* 2012, 24, 26−47

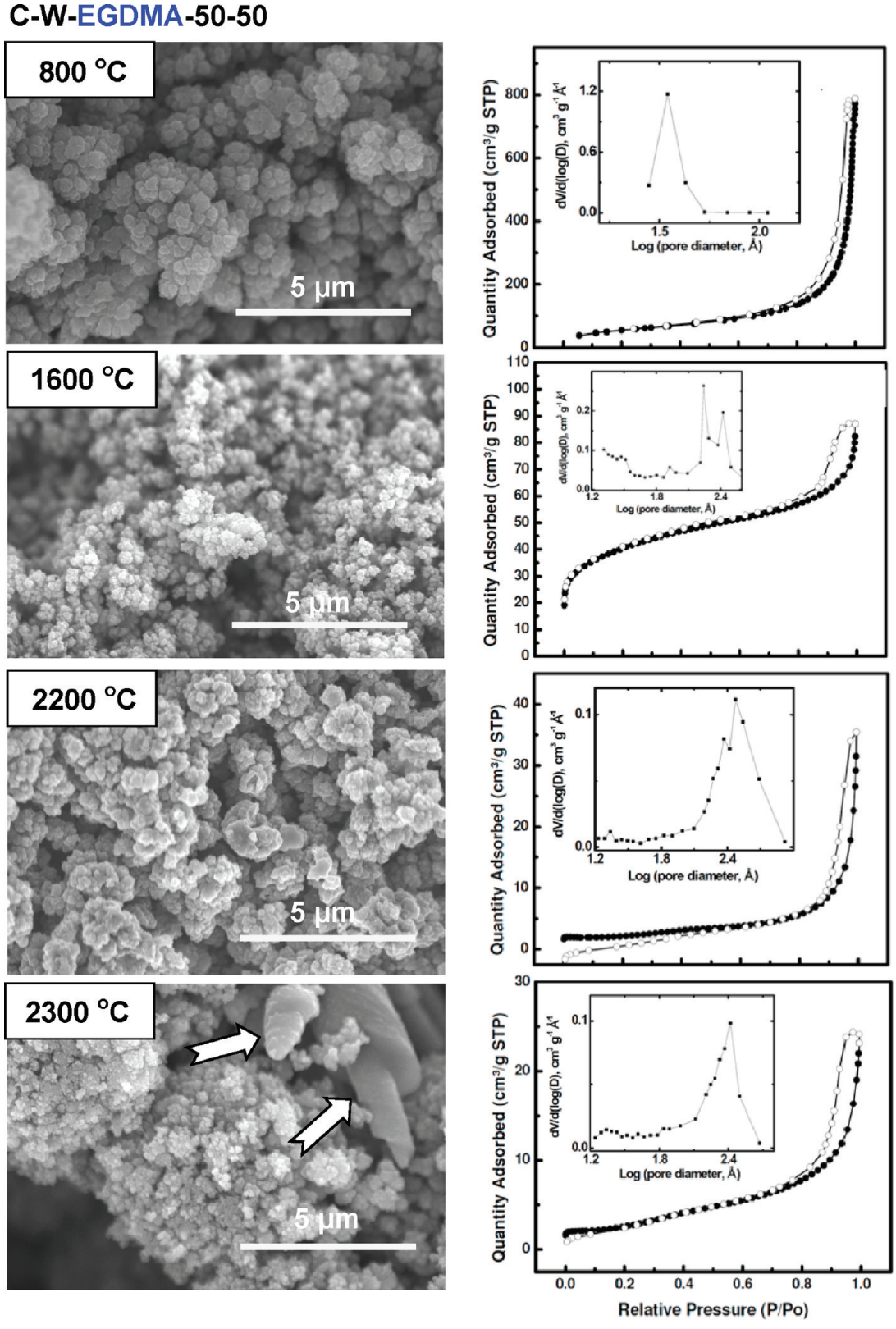

Figure 8. SEM and N_2-sorption data of a representative EGDMA-cross-linked PAN aerogel along treatment at progressively higher temperatures. (For the corresponding data with a representative HDDA-cross-linked sample see Figure S.3 in the Supporting Information.) Arrows show rod-like objects, present also in certain natural graphites (see text).

(compare ρ_b data in Table 7 with those in Tables 4 and 5). Skeletal densities, ρ_s, are between 1.72 g cm^{-3} and 1.92 g cm^{-3}, overlapping with the density range expected for amorphous carbon (1.8−2.0 g cm^{-3}).[55] Combination of ρ_b and ρ_s yields porosities in the range of 41−68% v/v, again not very different from those of the parent aerogels. Morphologically (by SEM, Figures 8 and S.3), all C-800 °C samples include macropores. However, quantitative analysis by N_2-sorption porosimetry

dx.doi.org/10.1021/cm202975p | *Chem. Mater.* 2012, 24, 26−47

Table 8. Evolution of the Materials Properties of Representative Carbon Aerogels As a Function of Processing Temperature and Cross-Linker

sample name-temperature (°C)	% weight loss	% linear shrinkage[a]	bulk density, ρ_b (g cm^{-3})	skeletal density, ρ_s (g cm^{-3})[b]	% porosity, Π	BET surface area, σ (m^2 g^{-1}) [c]	average pore diameter (nm)[d]	particle radius, r (nm)[e]	electrical conductivity (mho cm^{-1})[f]
Carbons from EGDMA- (**E**-) Cross-Linked PAN Aerogels									
C-W-E-50-50-800	[g]	[g]	0.71	1.834 ± 0.001	61	145 [23]	19 [24]	11.3	$4.5_6 \pm 0.6_1$
C-W-E-50-50-1600	15	3.0	0.70	$1.50_0 \pm 0.03_2$	53	143 [44]	6 [5.3]	14.0	$10._6 \pm 1._4$
C-W-E-50-50-2200	23	6.0	0.72	$1.40_1 \pm 0.03_5$	49	8 [1]	17 [338]	268	79 ± 10
C-W-E-50-50-2300	25	6.8	0.73	1.592 ± 0.007	54	10 [N/A]	9 [297]	188	139 ± 18
Carbons from HDDA- (**H**-) Cross-Linked PAN Aerogels									
C-W-H-50-50-800	[g]	[g]	0.63	1.781 ± 0.001	64	39 [7]	35 [105]	43.2	$1.4_8 \pm 0.1_6$
C-W-H-50-50-1600	15	4.0	0.63	$1.42_9 \pm 0.03_8$	56	58 [9]	7 [61]	36.2	$9.9_0 \pm 0.3_3$
C-W-H-50-50-2200	20	5.0	0.63	$1.53_9 \pm 0.01_1$	59	9 [N/A]	24 [417]	217	84.0 ± 0.9
C-W-H-50-50-2300	20	8.7	0.64	$1.64_6 \pm 0.02_2$	61	10 [N/A]	14 [382]	182	115 ± 23

[a]Relative to the 800 °C aerogel. [b]One sample, average of 50 measurements. [c]Numbers in brackets represent micropore surface areas in the same units. [d]By the $4 \times V_{Total}/\sigma$ method. For the first number, V_{Total} was calculated by the single-point adsorption method; for the number in brackets, V_{Total} was calculated via $V_{Total} = (1/\rho_b)\text{-}(1/\rho_s)$. [e]Calculated via $r = 3/\rho_s\sigma$. [f]Average of two samples, six measurements on each. [g]Those samples are the bases for the respective calculations.

holds surprises: either by the **W**-, or the **S**- route, carbons from the EGDMA-cross-linked (**E**-) samples show BET surface areas, σ, in the range of 137−300 m^2 g^{-1}, which is much higher than the range of their HDDA-cross-linked (**H**-) counterparts (41−62 m^2 g^{-1}). As a reminder, the same high/low relationship in the σ values was observed between the original **S**-**E**- and **S**-**H**-samples *but not* in the corresponding **W**-samples where all σ values were uniformly low, irrespective of the cross-linker (in the 25−40 m^2 g^{-1} range, Table 4). Further analysis of the N_2-sorption isotherms shows that pore diameters calculated by the $4V_{Total}/\sigma$ method using V_{Total} from $V_{Total} = (1/\rho_b)\text{-}(1/\rho_s)$, or from the highest point in the isotherm, are close to one another for the high surface area **C**-**W**-**E**- and **C**-**S**-**E**-samples, suggesting the presence of significant mesoporosity, which in turn justifies the higher BET surface areas. Higher surface areas, σ, for the **C**-**W**-**E**- and **C**-**S**-**E**-samples lead (via $r = 3/\rho_s\sigma$) to smaller particles (6−12 nm radius) relative to those for the **C**-**W**-**H**- and **C**-**S**-**H**-samples (25−53 nm radius). Thus, phenomenologically, the increase in the surface area observed with the **C**-**W**-**E**-samples may be explained by smaller particles. But the fundamental reasons are probably with the higher crystalline order imposed by EGDMA on the original PAN aerogels (see Figure 6): once the cross-linker is decomposed, the remnants of the PAN crystallites comprise cores of smaller carbon particles. Finally, samples processed at 800 °C are electrically conducting, as expected. **C**-**W**-**E**-**50**-**50**-**800** and **C**-**W**-**H**-**50**-**50**-**800** samples show conductivities equal to 4.6 ± 0.6 mho cm^{-1} and 1.5 ± 0.2 mho cm^{-1}, at ρ_b = 0.7 g cm^{-3} and ρ_b = 0.6 g cm^{-3}, respectively.

3.d.3. Graphitization of PAN-Derived Carbon Aerogels. Samples obtained by 800 °C carbonization were pyrolyzed further at 1600 °C and ultimately in the 2200−2300 °C range, and the resulting materials were compared with the original 800 °C forms. Since it was found that the materials properties of all 800 °C samples, **C**-**W**- and **C**-**S**-, depend only on the original cross-linker, **E**- or **H**-, not on the process, **W**- or **S**-, graphitization was conducted only with **W**-derived C-aerogels: **C**-**W**-**E**-**50**-**50**-**800** and **C**-**W**-**H**-**50**-**50**-**800**. Morphostructural changes were monitored by SEM and N_2-sorption porosimetry, chemical changes by elemental analysis, while graphitization was followed by XRD, Raman spectroscopy, and HRTEM. Data along graphitization are summarized in Table 8.

Compared with the 800 °C carbons, SEMs (Figures 8 and S.3) show that pyrolysis at 1600 °C results in finer-grained structures, followed by more coarse materials at 2200−2300 °C. All samples appear macroporous. In the 2300 °C samples, we also observe new micrometer-sized whisker-like objects (pointed by arrows) embedded in the surrounding particulate matter. Some of those whiskers are axially true; others possess a helical habit and resemble certain cone-like structures present in some natural graphites.[56] Similar structures have been observed in micrometer-size pores of glassy carbon of phenolic origin by carbonization at 2000 °C in a N_2 atmosphere and have been thought to originate from C−H(N_2) gas trapped in the pores during carbonization.[57] Analogous cone-like structures have also been produced from finely milled (for 24 h) natural graphite heated with epoxy in the 2100−2500 °C range. Under those conditions carbon is amorphous (reportedly ignites spontaneously in air), and the proposed mechanism involves CO-mediated growth.[58] However, none of those conditions are met in our case: as discussed below, already by 1600 °C our materials consist almost entirely of carbon (% w/w of N less than 1%), so we are rather inclined toward a more conventional screw dislocation mechanism.[59]

By N_2-sorption (Figures 8 and S.3), the volume adsorbed rises rapidly only above P/P_o = 0.9 confirming the macroporosity noted in all SEMs. Curiously, the 1600 °C samples also show a quick rise of the isotherm at low P/P_o values, suggesting microporosity (pores <2 nm). Indeed, while the overall BET surface area remains about constant between 800 and 1600 °C, *t*-plot analysis of the isotherms by the Harkins and Jura model[60] shows a significant increase of the micropore surface area. (This is particularly evident in the higher surface area **C**-**W**-**E**-**50**-**50** samples, where the micropore surface area about doubles from 23 m^2 g^{-1} at 800 °C to 44 m^2 g^{-1} at 1600 °C, see Table 8.) Chemical analysis (Table S.4) suggests an almost complete oxygen loss by 1600 °C, as the carbon content reaches 97.5% w/w. Therefore, the increase in microporosity is likely associated with a self-etching mechanism, whereas CO_2 generated internally comproportionates with carbon to CO. (That reaction is usually employed by introducing CO_2 externally in order to etch RF-derived C-aerogels and increase their surface area by a great amount.[61] Here, because of the stoichiometry of the situation, it takes place to a much lesser extent in situ.)

By the 2200−2300 °C range, traces of remaining oxygen have been lost and all samples, irrespective of their origin, consist of >99.5% w/w carbon (Table S.4). Despite the relatively small

dx.doi.org/10.1021/cm202975p | *Chem. Mater.* 2012, 24, 26−47

change in elemental composition between 1600 °C and the 2200−2300 °C range (97.6% to 99.7% w/w C by CHN analysis), certain materials properties change substantially (Table 8), consistent with growth of nano- and microcrystals. For example, while mass loss is compensated by shrinkage, hence ρ_b and Π values remain about the same as in the 800 °C samples (~0.6−0.7 g cm^{-3} and 49−64%, respectively), surface areas drop precipitously (to 8−10 m^2 g^{-1}), and average pore diameters and radii of the fundamental building blocks increase dramatically (from 61 to 417 nm and from 14 to 267 nm, respectively). Electrical conductivities (Table 8) increase progressively with the treatment temperature, reaching values over 100 mho cm^{-1} with ρ_b in the 0.6−0.7 g cm^{-3} range. Those values comprise an at least 5-fold improvement over the conductivity reported for RF-derived carbon aerogels at similar densities (~20 mho cm^{-1} at 0.65 g cm^{-3})[62a] and over 100-fold improvement over recently reported graphene aerogels, albeit at much lower densities (~1 mho cm^{-1} at 10 mg cm^{-3}).[62b] (Our conductivity measurements were also checked for their order-of-magnitude reliability by preparing RF-derived carbon aerogels via a nonaqueous acid-catalyzed route,[63] whose conductivity at 0.47 ± 0.01 g cm^{-3} was found equal to $2.4_8 \pm 0.1_7$ mho cm^{-1}).

Based on the above, in the 1600−2300 °C range we are dealing with annealing phenomena leading to reorganization of carbon. An immediate practical consequence is the presence of closed pores. This is inferred by the evolution of the skeletal densities, which first decrease as the treatment temperature increases, and then increase again, but overall stay below the ρ_s values at 800 °C (Table 8) and in the range for glassy carbon (1.5 g cm^{-3}),[64] that is lower than the density of graphite (2.26 g cm^{-3}).[55]

Direct evidence for graphitization comes from HRTEM (Figure 9). Irrespective of where we look at within the vast space surrounding rods in the terminal 2300 °C samples, we see intertwined ribbon-like crystallites of turbostratic carbon[65] with *d*-spacings (3.77−3.79 Å) near to that of the (002) planes of graphite (3.35 Å).[66] HRTEM images of samples treated at 800 °C, 1600 and 2200 °C are shown in Figure S.4 in the Supporting Information. (According to those, carbon aerogels obtained at 800 or 1600 °C show only minor graphitic order along the fringes of the samples.)

Quantitative evaluation of the structural evolution of carbon with treatment temperature was obtained with XRD and Raman spectroscopy. Figure 10 summarizes the data along with those from commercial carbon black and graphite. In XRD, the parent C-800 °C aerogels show two very broad bands in the general area for carbon (at 2θ around 25° and 45°), indicating amorphous material. As the treatment temperature increases, peaks become narrower, consistent with increasing crystallinity and formation of larger crystallites. Peaks at 26° and 42.5° correspond to the (002) and (101) diffractions of the hexagonal 2H graphite polymorph.[20a] The interlayer spacing, d_{002} (=l/(2 sin θ), Table 9), decreases and converges to the graphite spacing (3.35 Å).[66] The mean crystallite height, L_c, that is the along-the-*c*-axis mean stack height of graphene sheets comprising the graphite crystallites, was obtained by applying Scherrer's equation to the (002) diffraction peak. As the treatment temperature increases, L_c increases too (Table 9), but judging from the asymmetry of the diffraction peaks, it is concluded that we always have a mixture with less ordered carbon.

The crystallite width, L_a (crystallite size along the *a*-axis), is usually calculated via the Scherrer equation applied to the (100) diffraction peaks.[67] However, that diffraction is not prominent in the XRD spectra of graphite. Thus, for the calculation of L_a we resorted to Raman spectroscopy (Figure 10), wheres L_a is given by Knight's empirical formula (eq 5),[68] where λ_l is the laser wavelength in nm (632.8 nm here) and I_D and I_G are the integrated peak intensities (see below)

$$L_a(nm) = (2.4 \times 10^{-10})\lambda_l^4\left(\frac{I_D}{I_G}\right)^{-1} \quad (5)$$

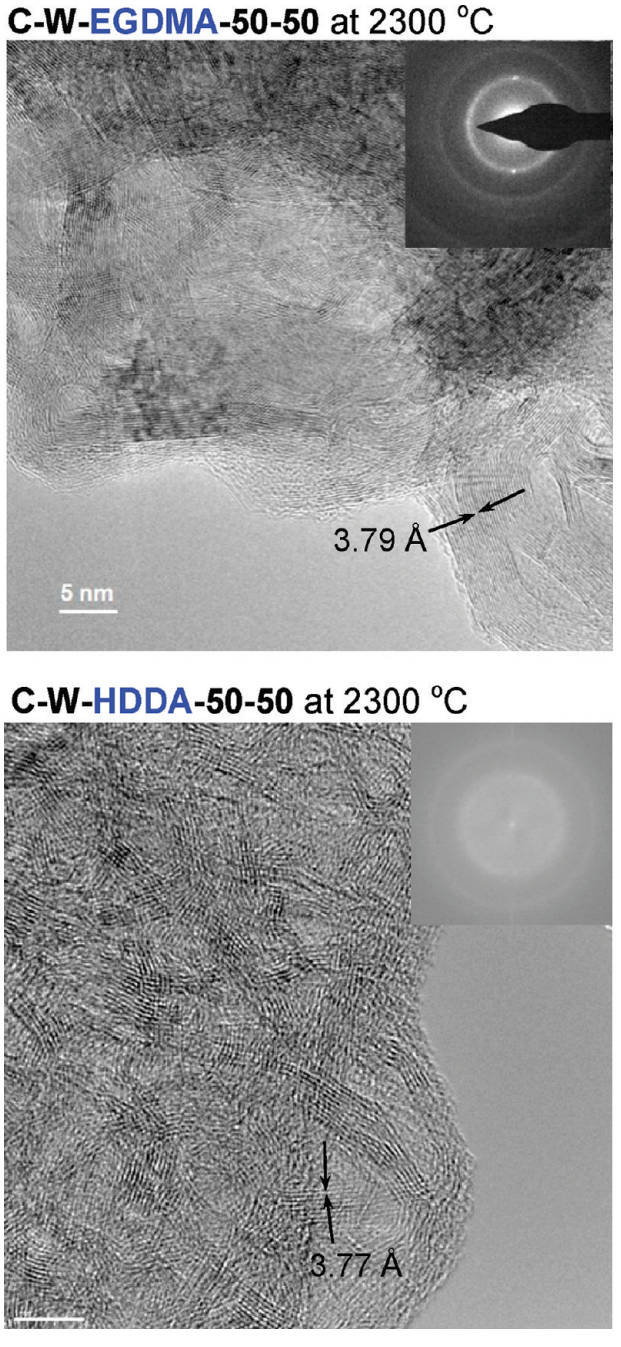

Figure 9. HRTEM of two emulsion-based samples made with EGDMA or HDDA cross-linkers after final graphitization treatment at 2300 °C. (HRTEM data after pyrolysis at 800 °C, 1600 and 2200 °C are included in Figure S.4 in the Supporting Information.) Insets: Upper, actual electron diffraction pattern; lower, diffraction pattern by Fourier transform of the image.

dx.doi.org/10.1021/cm202975p | *Chem. Mater.* 2012, 24, 26−47

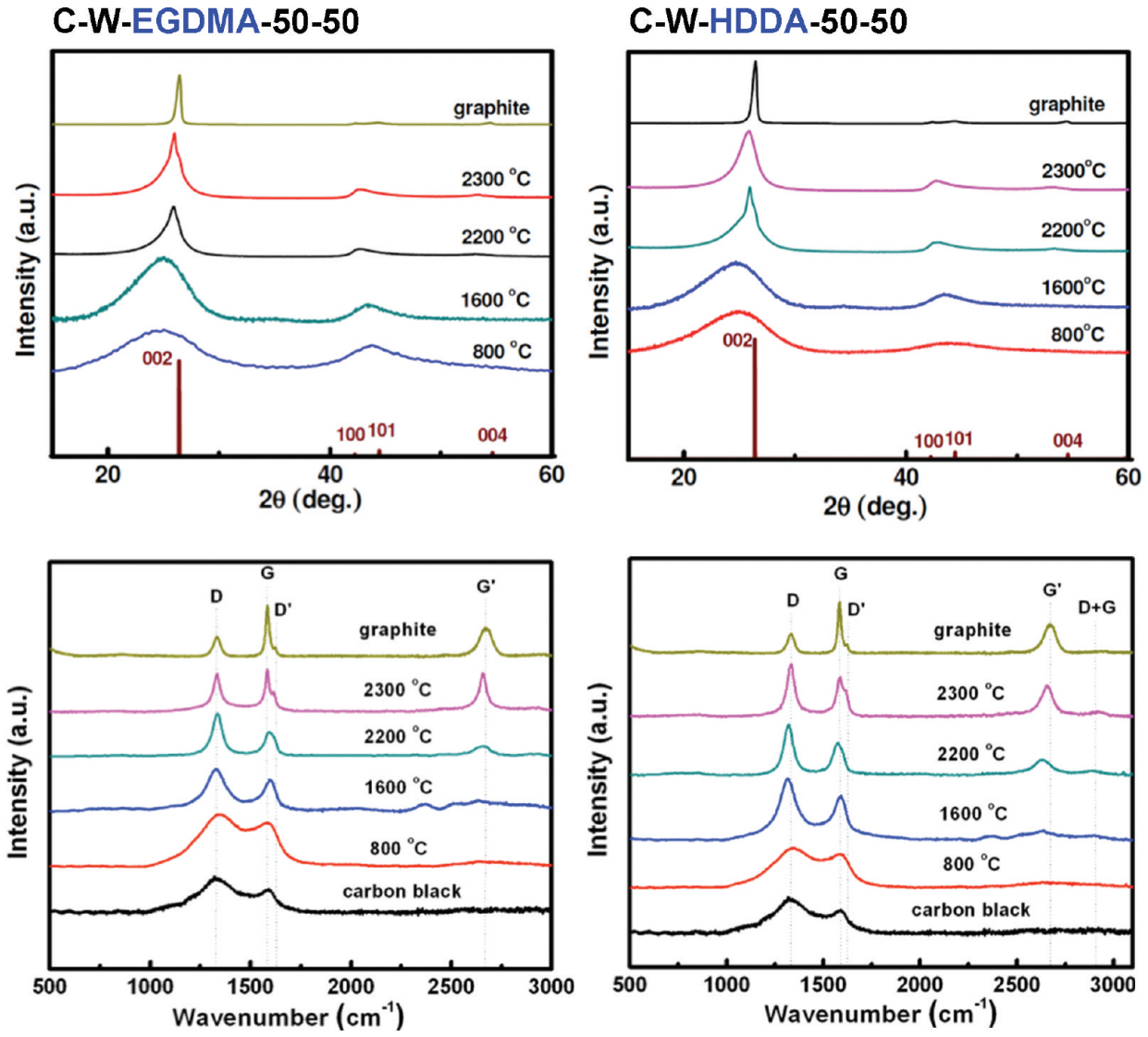

Figure 10. XRD and Raman data of two emulsion-based samples made with EGDMA or HDDA as cross-linkers after pyrolysis at the temperatures shown. (Data for commercial graphite and carbon black have been included for comparison.)

Table 9. XRD and Raman Data for Aerogels Treated at the Indicated Temperatures[a]

sample temperature (°C)	2 θ deg	d_{002} (nm)	L_c by XRD (Å)	I_D/I_G	L_a by Raman (nm)
graphite	26.44	0.337	208.1	0.198	194.4
carbon black				3.68	10.45
C-W-E-50-50 (EGDMA-Cross-Linked PAN)					
800	24.67	0.3601	10.7	2.64	14.58
1600	24.98	0.3561	14.9	2.15	17.89
2200	25.10	0.3442	42.5	1.77	21.74
2300	25.25	0.3424	38.1	1.15	33.46
C-W-H-50-50 (HDDA-Cross-Linked PAN)					
800	24.95	0.3566	11.4	2.78	13.84
1600	24.8	0.3585	13.6	1.63	23.60
2200	25.85	0.3443	29.8	1.58	24.36
2300	25.95	0.3438	43.2	1.45	26.54

[a]Data for commercial graphite and carbon black have been included for comparison.

At 800 °C, all Raman spectra closely resemble that of carbon black. Above 800 °C, all samples exhibit three dominant peaks associated with sp^2 carbon: a D peak at around 1350 cm^{-1} assigned to a breathing mode of A_{1g} symmetry (forbidden in perfect graphite and only allowed by disorder in defective graphite), a G peak at 1580 cm^{-1} assigned to the C−C bond stretching of E_{2g} symmetry (normal graphite structure), and a G′ peak at around 2700 cm^{-1} attributed to a second-order two-phonon process (present in all graphitic material).[69] As the treatment temperature increases, the G peak increases in intensity, and we observe a shoulder at around 1620 cm^{-1}, referred to as D′ peak and attributed to disorder.[70] In the present work, the major contributor to disorder is considered to be the grain boundaries in the microcrystalline graphite structure. The ratio of the integral intensities of the D and G Raman peaks, I_D/I_G, is a typical parameter used to quantify the degree of disorder in sp^2 carbons.[71] As shown in Table 9, as the treatment temperature increases the I_D/I_G ratio decreases, in agreement with increasing order. Eventually, at 2300 °C, the Raman spectrum of PAN aerogels using EGDMA as a cross-linker closely matches that of commercial graphite (see the Experimental Section). L_a values calculated via eq 5 are cited in Table 9.

dx.doi.org/10.1021/cm202975p | Chem. Mater. 2012, 24, 26–47

Overall, XRD and Raman data considered together suggest annealing of carbon into long (large L_a) and thin (smaller L_c) ribbon-like graphitic structures, in agreement with HRTEM. The process takes place efficiently above 2200 °C. As far as the graphite quality is concerned, all 2300 °C-samples are superior to aerospace-grade graphite fiber (compare data in Figure 10 with those in Figure S.5 in the Supporting Information). Graphitization is more efficient with PAN samples made with EGDMA as cross-linker (**E**-samples). Although the reasons should be related to the molecular rigidity and crystallinity imposed by that cross-linker in the parent PAN aerogels (Figure 6), it is also hard to speculate on the exact process.

4. CONCLUSIONS

Growing awareness of the environmental impact of chemical processing and the unavoidable transition from a growth to a sustainable economy render water-based, less energy-intensive processes not simply attractive but essential. The objective of using emulsion polymerization for the synthesis of PAN aerogels similar to their more conventional solution-polymerization counterparts was accomplished. With relatively high concentrations of monomer (AN), cross-linker (EGDMA or HDDA), and surfactants the process yields relatively large, by aerogel standards, primary particles that form macropores, thus reducing the surface tension forces and wet-gels are dried into aerogels from water under ambient pressure. PAN was specifically chosen, because it comprises the main nonphenolic source of carbon. Stepwise aromatization at 240 °C and carbonization at 800 °C yields amorphous carbons with significant residual amounts of N and O, whose materials properties differ only because of the cross-linker. Shorter, more rigid EGDMA yields 800 °C carbons with higher surface areas than longer, more flexible HDDA. By 1600 °C, all samples consist of >97% w/w carbon and have developed microporosity, attributed to a self-etching mechanism ($C + CO_2 \rightarrow 2\ CO$). By 2300 °C, samples consist of >99% w/w carbon and HRTEM shows ribbon-like graphitic structures. By XRD and Raman, carbons from EGDMA-cross-linked PAN show higher order than those from HDDA-cross-linked samples. Thus, remarkably, even though the cross-linker itself has been lost by 800 °C, there seems to be a memory effect whereas its molecular rigidity is transferred all the way to 2300 °C and is imprinted upon the crystalline order of the graphitized samples. Electrical conductivities reach values much higher than those of other sol−gel derived carbons.

Emulsion gelation is a viable route to organic aerogels. Unlike gelation by conventional solution polymerization, emulsions provide the means for multimodal particle size distributions (Figure S.1) that may be advantageous in terms of mechanical strength in certain applications (for example, refer to multigrained sandbags for blast mitigation[72]). As data reported here suggest, multimodal particle size distributions can be accessed by combining emulsion, suspension, and solution polymerization in one pot using suitable monomers, surfactants, and multiple (hydrophilic and lipophilic) initiators simultaneously. It is also certainly worth exploring tri- and tetrafunctional cross-linkers for increased interparticle connectivity, as well as polymerization schemes beyond the free-radical route of this report.

■ ASSOCIATED CONTENT

Supporting Information

Comparison of materials properties of **W-H-50-40** processed by irradiation only (no aging) at different times (Table S.1). Comparison of materials properties of **W**-aerogels dried under ambient pressure and with SCF CO_2 (Table S.2). Materials characterization data for the domain of the **S**-type samples (Table S.3). CHN elemental analysis data for selected **W**- and **S**-, **E**- and **H**-samples along the aromatization, carbonization, and graphitization processes (Table S.4). Heat capacity data for all **W**- and **S**-aerogels described in Tables 4 and 5 (Table S.5). SEM of control samples made of the **W-H-50-40** formulation with ***surf-AIBN*** playing the dual role of the initiator and the surfactant (Figure S.1). Typical mechanical characterization data under quasi-static compression (Figure S.2). SEM and N_2-soprtion data of a representative HDDA-cross-linked PAN aerogel as a function of pyrolysis temperature (Figure S.3). HRTEM at 800 °C, 1600 and 2200 °C of EGDMA and HDDA cross-linked aerogels (Figure S.4). XRD and Raman data of aerospace-grade graphite fiber (Figure S.5). This material is available free of charge via the Internet at http://pubs.acs.org.

■ AUTHOR INFORMATION

Corresponding Author

*E-mail: leventis@mst.edu (N.L.), cslevent@mst.edu (C.S.-L.), jtmang@lanl.gov (J.T.M.), kaan.kalkan@okstate.edu (A.K.K.), mfbertino@vcu.edu (M.F.B.).

■ ACKNOWLEDGMENTS

This project was supported by the Army Research Office under Award No. W911NF-10-1-0476 and the National Science Foundation under Agreement Nos. CHE-0809562 and CMMI-0653970. We also acknowledge the Materials Research Center of Missouri S&T for support in sample characterization (SEM, HRTEM, XRD). Solids NMR work was conducted at the University of Missouri Columbia by Dr. Wei Wycoff. This work benefited from the use of the SANS instrument, LQD at the Manuel Lujan, Jr. Neutron Scattering Center of the Los Alamos National Laboratory, supported by the DOE office of Basic Energy Sciences and utilized facilities supported in part by the National Science Foundation under Agreement No. DMR-0454672.

■ REFERENCES

(1) (a) Lee, J.; Kim, J.; Hyeon, T. *Adv. Mater.* **2006**, *18*, 2073−2094. (b) Kuchta, B.; Firlej, L.; Pfeifer, P.; Wexler, C. *Carbon* **2010**, *48*, 223−231.

(2) (a) Antolini, E. *Appl. Catal., B* **2009**, *88*, 1−24. (b) Stüber, F.; Font, J.; Fortuny, A.; Bengoa, C.; Eftaxias, A.; Fabregat, A. *Top. Catal.* **2005**, *33*, 3−50.

(3) (a) Liang, C.; Li, Z.; Dai, S. *Angew. Chem., Int. Ed.* **2008**, *47*, 3696−3717. (b) White, R. J.; Budarin, V.; Luque, R.; Clark, J. H.; Macquarriea, D. J. *Chem. Soc. Rev.* **2009**, *38*, 3401−3418. (c) Hanai, T. *J. Chromatogr., A* **2003**, *989*, 183−196.

(4) (a) Lee, J.; Kim, J.; Hyeon, T. *Adv. Mater.* **2006**, *18*, 2073−2094. (b) Lee, J.; Kim, J.; Hyeon, T. *Adv. Mater.* **2006**, *18*, 2073−2094. (c) Wan, Y.; Shi, Y.; Zhao, D. *Chem. Mater.* **2008**, *20*, 932−945. (d) Zainoodin, A. M.; Kamarudin, S. K.; Daud, W. R. W. *Int. J. Hydrogen Energy* **2010**, *35*, 4606−4621.

(5) Kabbour, H.; Baumann, T. F.; Satcher, J. H.; Saulnier, A.; Ahn, C. C. *Chem. Mater.* **2006**, *18*, 6085−6087.

(6) (a) Brinker, C. J.; Scherer, G. W. *Sol-gel Science. The Physics and Chemistry of Sol-gel Processing*; Academic Press: New York, 1990. (b) Hüsing, N.; Schubert, U. *Angew. Chem., Int. Ed.* **1998**, *37*, 22−45.

(c) Morris, C. A.; Anderson, M. L.; Stroud, R. M.; Merzbacher, C. I.; Rolison, D. R. *Science* **1999**, *284*, 622−624. (d) Pierre, A. C.; Pajonk, G. M. *Chem. Rev.* **2002**, *102*, 4243−4265.
(7) Biesmans, G.; Mertens, A.; Duffours, L.; Woignier, T.; Phalippou, J. *J. Non-Cryst. Solids* **1998**, *225*, 64−68.
(8) Leventis, N.; Sotiriou-Leventis, C.; Chandrasekaran, N.; Mulik, S.; Larimore, Z. J.; Lu, H.; Churu, G.; Mang, J. T. *Chem. Mater.* **2010**, *22*, 6692−6710.
(9) (a) Lorjai, P.; Chaisuwan, T.; Wongkasemjit, S. *J. Sol-Gel Sci. Technol.* **2009**, *52*, 56−64. (b) Katanyootaa, P.; Chaisuwana, T.; Wongchaisuwatb, A.; Wongkasemjita, S. *Mater. Sci. Eng., B* **2010**, *167*, 36−42.
(10) (a) Rhine, W.; Wang, J.; Begag, R. Polyimide aerogels, carbon aerogels, and metal carbide aerogels and methods of making same, U.S. Patent No. 7,074,880 (2006). (b) Chidambareswarapattar, C.; Larimore, Z.; Sotiriou-Leventis, C.; Mang, J. T.; Leventis, N. *J. Mater. Chem.* **2010**, *20*, 9666−9678.
(11) Ritter, J. A.; Al-Muhtaseb, S. A. *Adv. Mater.* **2003**, *15*, 101−114.
(12) (a) Pekala, R. W. *J. Mater. Sci.* **1989**, *24*, 3221−3227. (b) Pekala, R. W.; Alviso, C. T.; Kong, F. M.; Hulsey, S. S. *J. Non-Cryst. Solids* **1992**, *145*, 90−98. (c) Lu, X.; Arduini-Schuster, M. C.; Kuhn, J.; Nilsson, O.; Fricke, J.; Pekala, R. W. *Science* **1992**, *255*, 971−972. (d) Pekala, R. W. U.S. Patent 4,873,218 (1989). (e) Pekala, R. W.; Schaefer, D. W. *Macromolecules* **1993**, *26*, 5887−5893. (f) Saliger, R.; Bock, V.; Petricevic, R.; Tillotson, T.; Geis, S.; Fricke, J. *J. Non-Cryst. Solids* **1997**, *221*, 144−150. (g) Lu, X.; Caps, R.; Fricke, J.; Alviso, C. T.; Pekala, R. W. *J. Non Cryst. Solids* **1995**, *188*, 226−234. (h) Lin, C.; Ritter, J. A. *Carbon* **1997**, *35*, 1271−1278. (i) Job, N.; Panariello, F.; Marien, J.; Crine, M.; Pirard, J.-P.; Leonard, A. *J. Non-Cryst. Solids* **2006**, *352*, 24−34.
(13) Baumann, T. F.; Worsley, M. A.; Han, T. Y. J.; Satcher, J. H. Jr. *J. Non-Cryst. Solids* **2008**, *354*, 3513−3515.
(14) Gierszal, K. P.; Jaroniec, M. *J. Am. Chem. Soc.* **2006**, *128*, 10026−10027.
(15) Tanaka, S.; Katayama, Y.; Tate, M. P.; Hillhouse, H. W.; Miyake, Y. *J. Mater. Chem.* **2007**, *17*, 3639−3645.
(16) Cross, A. F.; Nowak, A. P. *Langmuir* **2010**, *26*, 11378−11383.
(17) Mulik, S.; Sotiriou-Leventis, C.; Leventis, N. *Chem. Mater.* **2008**, *20*, 6985−6997.
(18) Balbuena, P. B.; Wang, Y. *Lithium-Ion Batteries: Solid-Electrolyte Interphase*, First ed; Imperial College Press: Covent Garden, London, 2007.
(19) (a) Oberlin, A.; Roucky, J. P. *Carbon* **1971**, *9*, 39−42. (b) Audier, M.; Oberlin, A.; Oberlin, M.; Coulon, M.; Bonneatin, L. *Carbon* **1981**, *19*, 217−224. (c) Inagaki, M.; Okada, Y.; Vignal, V.; Komo, H.; Oshida, K. *Carbon* **1998**, *36*, 1706−1708. (d) Lei, Z.; Xiao, Y.; Dang, L.; You, W.; Hu, G.; Zhang, J. *Chem. Mater.* **2007**, *19*, 477−484.
(20) (a) Maldonado-Hódar, F. J.; Moreno-Castilla, C.; Rivera-Utrilla, J.; Hanzawa, Y.; Yamada, Y. *Langmuir* **2000**, *16*, 4367−4373. (b) Fu, R.; Baumann, T. F.; Cronin, S.; Dresselhaus, G.; Dresselhaus, M. S.; Satcher, J. H. Jr. *Langmuir* **2005**, *21*, 2647−2651.
(21) (a) Leventis, N.; Chandrasekaran, N.; Sotiriou-Leventis, C.; Mumtaz, A. *J. Mater. Chem.* **2009**, *19*, 63−65. (b) Leventis, N.; Chandrasekaran, N.; Sadekar, A. G.; Mulik, S.; Sotiriou-Leventis, C. *J. Mater. Chem.* **2010**, *20*, 7456−7471.
(22) Morgan, P. *Carbon Fibers and Their Composites*; CRC Press: Boca Raton, FL, 2005.
(23) (a) Everett, D. H. *Basic Principles of Colloid Science*; The Royal Society of Chemistry: London, U.K., 1988; p 32. (b) Everett, D. H. *Basic Principles of Colloid Science*; The Royal Society of Chemistry: London, U.K., 1988; p 189.
(24) Kistler, S. S. *J. Phys. Chem.* **1932**, *36*, 52−64.
(25) Daniel, C.; Giudiee, S.; Guerra, G. *Chem. Mater.* **2009**, *21*, 1028−1034.
(26) (a) Fischer, F.; Rigacci, A.; Pirard, R.; Berthon-Fabry, S.; Achard, P. *Polymer* **2006**, *47*, 7636−7645. (b) Gavillon, R.; Budtova, T. *Biomacromolecules* **2008**, *9*, 269−277. (c) Surapolchai, W.; Schiraldi, D. A. *Polym. Bull.* **2010**, *65*, 951−960.
(27) Goueree, P.; Talbi, H.; Miousse, D.; Tran-van, F.; Dao, L. H.; Lee, K. H. *J. Electrochem. Soc.* **2001**, *148*, A94−A101.
(28) This speculation is based on the recently reported mechanical properties of fibrous nanostructures. See for example ref 8, as well as the following: Leventis, N.; Sotiriou-Leventis, C.; Mulik, S.; Dass, A.; Schnobrich, J.; Hobbs, A.; Fabrizio, E. F.; Luo, H.; Churu, G.; Zhang, Y.; Lu, H. *J. Mater. Chem.* **2008**, *18*, 2475−2482.
(29) (a) Bordjiba, T.; Mohamedi, M.; Dao, L. H. *J. Power Sources* **2007**, *172*, 991−998. (b) Bordjiba, T.; Mohamedi, M.; Dao, L. H. *Adv. Mater.* **2008**, *20*, 815−819.
(30) For a recent discussion, see: Leventis, N.; Chidambareswarapattar, C.; Mohite, D. P.; Larimore, Z. J.; Lu, H.; Sotiriou-Leventis, C. *J. Mater. Chem.* **2011**, *21*, 11981−11986.
(31) (a) Vlakh, E. G.; Tennikova, T. B. *J. Sep. Sci.* **2007**, *30*, 2801−2813. (b) Urban, P.; Jandera, P. *J. Sep. Sci.* **2008**, *31*, 2521−2540.
(32) See for example: Bajpai, A. K. *J. Mater. Sci.: Mater. Med.* **2008**, *19*, 343−357, related to biocompatible gels.
(33) Odian, G. *Principles of Polymerization*, Fourth ed.; John Wiley and Sons: Hoboken, NJ, USA, 2004; Chapter 4, p 350.
(34) (a) Bisson, A; Rigacci, A.; Lecomte, D.; Rodier, E.; Achard, P. *Drying Technol.* **2003**, *21*, 593−628. (b) Pakowski, Z. *Drying 2004 - Proceedings 14th IDS 2004*, 2004, *A*, 69−88. (c) Wu, D.; Fu, R. *J. Porous Mater.* **2008**, *15*, 29−34.
(35) Liu, N.; Zhang, S.; Fu, R.; Dresselhaus, M. S.; Dresselhaus, G. *J. Appl. Polym. Sci.* **2007**, *104*, 2849−2855.
(36) See for example: (a) Amatani, T.; Nakanishi, K.; Hirao, K.; Kodaira, T. *Chem. Mater.* **2005**, *17*, 2114. (b) Leventis, N.; Mulik, S.; Wang, X.; Dass, A.; Patil, V. U.; Sotiriou-Leventis, C.; Lu, H.; Churu, G.; Capecelatro, A. *J. Non-Cryst. Solids* **2008**, *354*, 632−644. (c) Leventis, N.; Mulik, S.; Wang, X.; Dass, A.; Sotiriou-Leventis, C.; Lu, H. *J. Am. Chem. Soc.* **2007**, *129*, 10660−10661.
(37) Cohen, N.; Silverstein, M. S. *Polymer* **2011**, *52*, 282−287.
(38) Antonietti, M.; Caruso, R. A.; Goltner, C. G.; Weissenberger, M. C. *Macromolecules* **1999**, *32*, 1383−1389.
(39) Wardencki, W.; Curylo, J.; Namiesnik, J. *Polish J. Environ. Studies* **2005**, *14*, 389−395.
(40) Seeger, P. A.; Hjelm, R. P. Jr. *J. Appl. Crystallogr.* **1991**, *24*, 467−478.
(41) Geometric Factors in Four Point Resistivity Measurements, Bulletin No. 472-13, Haldor Topsoe Semiconductor Division: Vedbæk, May 25, 1968, p 37. See, also: http://www.fourpointprobes.com/haldor.html (accessed December 10, 2011).
(42) Dobbins, H. M.; Peck, E. R. *J. Opt. Soc. Am.* **1973**, *63*, 318−320.
(43) (a) Bowcott, J. E.; Schulman, J. H. *Z. Elecktrochem* **1955**, *59*, 283−288. (b) Osipow, L. L.; Rosenblatt, W. *J. Am. Oil Chem. Soc.* **1967**, *44*, 307−309.
(44) Kotlarchyk, M.; Chen, S.-H.; Huang, J. S.; Kim, M. W. *Phys. Rev. Lett.* **1984**, *53*, 941−944.
(45) Ashcroft, W.; Lekner, J. *Phys. Rev.* **1966**, *145*, 83−90.
(46) (a) Beaucage, G. *J. Appl. Crystallogr.* **1995**, *28*, 717−728. (b) Beaucage, G. *J. Appl. Crystallogr.* **1996**, *29*, 134−146. (c) Mang, J. T.; Son, S. F.; Hjelm, R. P.; Peterson, P. D.; Jorgensen, B. S. *J. Mater. Res.* **2007**, *22*, 1907−1920. (d) Tappan, B. C.; Huynh, M. H.; Hiskey, M. A.; Chavez, D. E.; Luther, E. P.; Mang, J. T.; Son, S. F. *J. Am. Chem. Soc.* **2006**, *128*, 6589−6594.
(47) Leventis, N.; Sotiriou-Leventis, C.; Mohite, D. P.; Larimore, Z. J.; Mang, J. T.; Churu, G.; Lu, H. *Chem. Mater.* **2011**, *23*, 2250−2261.
(48) Schelten, J.; Schmatz, W. *J. Appl. Crystallogr.* **1980**, *13*, 385−390.
(49) Hurley, R. B.; Tzentis, L. S. *Polym. Lett.* **1963**, *1*, 423−426.
(50) (a) Leventis, N.; Sotiriou-Leventis, C.; Zhang, G.; Rawashdeh, A.-M. M. *Nano Lett.* **2002**, *2*, 957−960. (b) Leventis, N.; Palczer, A.; McCorkle, L.; Zhang, G.; Sotiriou-Leventis, C. *J. Sol-Gel Sci. Technol.* **2005**, *35*, 99−105. (c) Leventis, N. *Acc. Chem. Res.* **2007**, *40*, 874−884. (d) Mulik, S.; Sotiriou-Leventis, C.; Churu, G.; Lu, H.; Leventis, N. *Chem. Mater.* **2008**, *20*, 5035−5046.
(51) Consequently, also the ability of the **S**-samples to store energy (a measure of toughness) is much higher - see Table 6. It is further noted, however, that neither the ultimate strain, nor the ultimate stress, nor the specific energy absorption even of the **S**-aerogels is as high as

to what has been measured for polymer cross-linked silica aerogels at similar densities,[50] or for other all-polymer aerogels (e.g., polyurea,[8] ROMP-derived polyimides,[47] or polyamide aerogels[30]). On the other hand, the low values of the Young's modulus of the **W**-aerogels result in very low values for the speed of sound (included in Table 6) and render **W**-aerogels worth evaluating for applications in acoustic insulation.

(52) (a) Rahaman, M. S. A.; Ismail, A. F.; Mustafa, A. *Polym. Degrad. Stab.* **2007**, *92*, 1421−1432. (b) Usami, T.; Itoh, T.; Ohtani, H.; Tsuge, S. *Macromolecules* **1990**, *23*, 2460−2465.

(53) (a) Li, J.; Huang, X.; Chen, L. *J. Electrochem. Soc.* **2000**, *147*, 2653−2657. (b) Tan, L.; Wan, A.; Pan, D. *Mater. Lett.* **2011**, *65*, 887−890.

(54) Wang, Y.-X.; Wang, Q. *J. Appl. Polym. Sci.* **2007**, *104*, 1255−1259.

(55) McKenzie, D. R.; Muller, D.; Pailthorpe, B. A. *Phys. Rev. Lett.* **1991**, *67*, 773−776.

(56) (a) Jaszczak, J. A.; Dimovski, S.; Hackney, S. A.; Robinson, G. W.; Bosio, P.; Gogotsi, Y. *Can. Mineral.* **2007**, *45*, 379−389. (b) Jaszczak, J. A.; Robinson, G. W.; Dimovski, S.; Gogotsi, Y. *Carbon* **2003**, *41*, 2085−2092.

(57) Gogotsi, Y.; Libera, J. A.; Kalashnikov, N.; Yoshimura, M. *Science* **2000**, *290*, 317−320.

(58) Dong, J.; Shen, W.; Zhang, B.; Liu, X.; Kang, F.; Gu, J.; Li, D.; Chen, N. *Carbon* **2001**, *39*, 2325−2333.

(59) (a) Bennema, P. *J. Cryst. Growth* **1984**, *69*, 182−197. (b) Burton, W. K.; Cabrera, N.; Frank, F. C. *Nature* **1949**, *163*, 398−399.

(60) Webb, P. A.; Orr, C. *Analytical Methods in Fine Particle Technology*; Micromeritics Instrument Corporation: Norcross, GA, U.S.A., 1997; pp 67−68.

(61) Singh, A.; Lal, D. *J. Appl. Polym. Sci.* **2010**, *115*, 2409−2415.

(62) (a) Lu, X.; Nilsson, O.; Fricke, J.; Pekala, R. W. *J. Appl. Phys.* **1993**, *73*, 581−584. (b) Worsley, M. A.; Pauzauskie, P. J.; Olson, T. Y.; Biener, J.; Satcher, J. H. Jr.; Baumann, T. F. *J. Am. Chem. Soc.* **2010**, *132*, 14067−14069.

(63) Mulik, S.; Sotiriou-Leventis, C.; Leventis, N. *Chem. Mater.* **2007**, *19*, 6138−6144.

(64) (a) Salamone, J. C. *Concise Polymeric Materials Encyclopedia*; CRC Press: Boca Raton, FL, U.S.A., 1999; p 570. (b) Pierson, H. O. *Handbook of carbon, graphite, diamond and fullerenes*; Noyes Publications: Park Ridge, NJ, U.S.A., 1993; p 131.

(65) Ban, L. L.; Crawford, D.; Marsh, H. *J. Appl. Crystallogr.* **1975**, *8*, 415−420.

(66) Pierson, H. O. *Handbook of Carbon, Graphite, Diamond and Fullerenes*; Noyes Publications: New Jersey, U.S.A., 1993.

(67) Kercher, A. K.; Nagle, D. C. *Carbon* **2003**, *41*, 15−27.

(68) Cançado, L. G.; Takai, K.; Enoki, T.; Endo, M.; Kim, Y. A.; Mizusaki, H.; Jorio, A.; Coelho, L. N.; Magalhães-Paniago, R.; Pimenta, M. A. *Appl. Phys. Lett.* **2006**, *88*, 163106/1−3.

(69) It is noted that the band labeled as G′ has also been referred to as 2D, and it has been considered as the second overtone of the D band. See, for example: (a) Tan, P.; Dimovski, S.; Gogotsi, Y. *Philos. Trans. R. Soc. London, Ser. A* **2004**, *362*, 2289−2310. (b) Ferrari, A. C.; Meyer, J. C.; Scardaci, V.; Casiraghi, C.; Lazzeri, M.; Mauri, F.; Piscanec, S.; Jiang, D.; Novoselov, K. S.; Roth, S.; Geim, A. K. *Phys. Rev. Lett.* **2006**, *97*, 187401/1−4. (c) Dresselhaus, M. S.; Dresselhaus, G.; Saito, R.; Jorio, A. *Phys. Rep.* **2005**, *409*, 47−99. However, there are several difficulties in the assignment of that peak to the second overtone of the D peak: (i) the frequency of the G′ peak is not precisely twice that of the D-peak frequency; (ii) as the disorder increases, the D band increases, but the G′ band decreases, and vice versa; and, (iii) one of the elastic scattering events, which appears in the one-phonon emission spectra in the D (D′) mode does not exist in the two-phonon emission Raman spectra in the G (G′) mode. Indeed, it has been argued in the recent literature that the peak at ∼2650 cm^{-1} is not a defect-induced feature and is assigned the G′ notation. The G′ peak is assigned to a two-phonon scattering process (an intervalley scattering process), which connects two high symmetry points, K and K′, of the first Brillouin zone: (a) Dresselhaus, M. S.; Jorio, A.; Hofmann, M.; Dresselhaus, G.; Saito, R. *Nano Lett.* **2010**, *10*, 751−758. (b) Jorio, A.; Dresselhaus, M. S.; Saito, R.; Dresselhaus, G. F. *Raman Spectroscopy in Graphene Related Systems*; Wiley-VCH Verlag GmbH & Co. KGaA: Weinheim, Germany, 2011. (c) Saito, R.; Hofmann, M.; Dresselhaus, G.; Jorio, A.; Dresselhaus, M. S. *Adv. Phys.* **2011**, *60*, 413−550.

(70) Nemanich, R. J.; Solin, S. A. *Phys. Rev. B* **1979**, *20*, 392−401.

(71) Ko, T.-H. *J. Appl. Polym. Sci.* **1996**, *59*, 577−580.

(72) See, for example: (a) Daphalapurkar, N. P.; Wang, F.; Fu, B.; Lu, H.; Komanduri, R. *Exp. Mech.* **2011**, *51*, 719−728. (b) Hogg, P. J. *Science* **2006**, *314*, 1100−1101.